A nodal high-order discontinuous Galerkin method for elastic wave propagation in arbitrary heterogeneous media

E. Diego Mercerat, Nathalie Glinsky

Geophysical Journal International

Geophys. J. Int. (2015) **201,** 1101–1118
GJI Seismology

doi: 10.1093/gji/ggv029

A nodal high-order discontinuous Galerkin method for elastic wave propagation in arbitrary heterogeneous media

E. Diego Mercerat[1] and Nathalie Glinsky[1,2,3]

[1] *CEREMA Direction Territoriale Méditerranée, Nice, France. E-mail: diego.mercerat@cerema.fr*
[2] *IFSTTAR – Université Paris Est, Marne la Vallée, France*
[3] *INRIA Sophia Antipolis Méditerranée, France*

Accepted 2015 January 15. Received 2015 January 12; in original form 2014 August 26

SUMMARY

We present an extension of the nodal discontinuous Galerkin method for elastic wave propagation to high interpolation orders and arbitrary heterogeneous media. The high-order lagrangian interpolation is based on a set of nodes with excellent interpolation properties in the standard triangular element. In order to take into account highly variable geological media, another set of suitable quadrature points is used where the physical and mechanical properties of the medium are defined. We implement the methodology in a 2-D discontinuous Galerkin solver. First, a convergence study confirms the *hp*-convergence of the method in a smoothly varying elastic medium. Then, we show the advantages of the present methodology, compared to the classical one with constant properties within the elements, in terms of the complexity of the mesh generation process by analysing the seismic amplification of a soft layer over an elastic half-space. Finally, to verify the proposed methodology in a more complex and realistic configuration, we compare the simulation results with the ones obtained by the spectral element method for a sedimentary basin with a realistic gradient velocity profile. Satisfactory results are obtained even for the case where the computational mesh does not honour the strong impedance contrast between the basin bottom and the bedrock.

Key words: Earthquake ground motions; Computational seismology; Wave propagation.

1 INTRODUCTION

In the recent years, advances in computer architectures render large-scale seismic wave propagation simulations feasible in 3-D highly heterogeneous media. Several numerical methods are available and the final choice is clearly problem dependant. The reader is referred to Wu *et al.* (2007), Robertsson *et al.* (2007), Virieux *et al.* (2012) and Moczo *et al.* (2014) for thorough reviews of the many different techniques currently available for seismic modelling.

Among them, the methodologies based on the variational formulation of elastodynamics allow for accurate implementation of boundary conditions through structured or unstructured meshes. They can be grouped into two main categories: (1) those which impose the continuity of the solution field between neighbouring elements, what are known as the finite (low-order) or spectral (high-order) element methods (Seriani & Priolo 1994; Bao *et al.* 1998; Komatitsch & Vilotte 1998; Karniadakis & Sherwin 1999) and (2) those which do not impose the continuity but instead allow discontinuities of the field between neighbouring elements, which are named discontinuous Galerkin (DG) finite element methods (DG-FEM; Käser & Dumbser 2006; De Basabe & Sen 2007; Delcourte *et al.* 2009; Etienne *et al.* 2010; Tago *et al.* 2012). Both methodologies have been successfully applied to simulate fault rupture dynamics (Käser *et al.* 2007b; Olsen *et al.* 2008; Benjemaa *et al.* 2009; Stupazzini *et al.* 2009; Tago *et al.* 2012), seismic wave propagation (Dumbser *et al.* 2007; Etienne *et al.* 2010; De Martin 2011; Peter *et al.* 2011; Cupillard *et al.* 2012; Mazzieri *et al.* 2013) and site effects studies (Bielak *et al.* 2003; Xu *et al.* 2003; Taborda *et al.* 2012; Peyrusse *et al.* 2014). In this work, we place ourselves in the DG framework, although we note that the proposed methodology to handle arbitrary heterogeneous media is independent of how the communication between elements is established. In fact, it is inspired by the multidimensional lagrangian interpolation combined with high-order integration rules currently used in many finite element techniques (Karniadakis & Sherwin 1999; Pasquetti & Rapetti 2006; De Basabe *et al.* 2008; Seriani & Su 2012; Lazar *et al.* 2013; Mazzieri *et al.* 2013).

High-order finite element methods in unstructured triangular meshes have been applied to solve seismic wave propagation (Cohen *et al.* 2001; Komatitsch *et al.* 2001; Mercerat *et al.* 2006; Mazzieri & Rapetti 2012). Recently, their dispersion characteristics have been shown to be very similar to their hexahedral counterpart (Mercerat *et al.* 2006; De Basabe *et al.* 2008; Liu *et al.* 2012; Mazzieri & Rapetti 2012) when the mass matrix is analytically calculated. The main caveat of these methodologies lies on the inefficiency linked to the global mass matrix inversion at each time step, when an

explicit time-scheme is used to solve the semi-discrete problem, as is common practice in computational seismology. For this reason, the DG method happens to be a valuable alternative, as all calculations are done at the local level (i.e. no global mass matrix assembling). On the contrary, the fluxes between neighbouring elements must be accounted for and many different strategies have been studied in the literature (Cockburn *et al.* 2000; Hesthaven & Warburton 2008).

Since the numerous papers on the DG method applied to seismic waves modelling (Käser & Dumbser 2006; de la Puente *et al.* 2007; Dumbser *et al.* 2007; Hermann *et al.* 2011), the modal approach has become quite popular. It consists of the expansion of the solution field on the hierarchical basis of orthogonal polynomials in the standard elements (triangles in 2-D, tetrahedra in 3-D) and also the analytical calculation of local mass and stiffness matrices. In most of these studies, the discretization is based on the assumption of constant material properties inside mesh elements. Although, in order to account for variable physical properties within the elements, additional terms and a new set of stiffness matrices must be considered (Castro *et al.* 2010). On the contrary, the nodal DG method (Hesthaven & Warburton 2008) lies on the lagrangian interpolation of the solution field within each element of the mesh and the integration of local matrices, either analytically (Delcourte *et al.* 2009) or by quadrature rules in the general case. Thus, a suitable set of interpolation and quadrature nodes are required. The polynomial basis is no longer hierarchical, but it provides readable expressions of the numerical fluxes calculated on the element edges (lines in 2-D and triangular facets in 3-D domains). The cardinality property of the nodal basis allows to use information just along the element edges to compute the integrals needed for flux calculations. In 3-D simulations, this implies a complexity of $\mathcal{O}(N^2)$ for the nodal, instead of $\mathcal{O}(N^3)$ for the modal approach (Hesthaven & Warburton 2008). Nodal DG-FEMs have been already applied for elastic waves modelling by Delcourte *et al.* (2009), Etienne *et al.* (2010), Delcourte & Glinsky (2015) and by Peyrusse *et al.* (2014) for viscoelastic media, though restricted to low interpolation orders. Nevertheless, it should be stressed that for low or moderate interpolation orders (less than 6), as is common practice in computational seismology, the differences in computational cost between the modal and the nodal approaches are less significant. A thorough study, specially in large-scale 3-D simulations, is still missing.

High-order methods allow, in principle, to introduce element sizes much longer than the minimum propagated wavelength. As classical in SEM, a typical element of moderate degree (order 4 or 5) must be of the order of the minimum propagated wavelength to obtain an acceptable solution (Faccioli *et al.* 1997; Komatitsch & Vilotte 1998; Basabe & Sen 2007; Seriani & Oliveira 2008). Similar element sizes are preconized in the modal DG approach (Dumbser & Käser 2006; Wenk *et al.* 2013). However, the need to correctly sampling strongly heterogeneous media (specially near the surface) may require meshes with elements on the order of metres, or even less. This is clearly not feasible with methods based of the hypothesis of constant material properties per element. The question also arises in collocated methods, such as classical SEM, about the effect of a strong impedance contrast inside an element on the accuracy of the final seismograms. The recent study by Seriani & Su (2012) proposes a *poly-grid* methodology to take into consideration sharp velocity contrasts within the elements of the mesh. In some way, we follow a similar strategy here using two different grids: one for the interpolation and other for the numerical integration, that can have in principle as many degrees of freedom as necessary to correctly represent an arbitrary medium.

In this study, we extend the nodal DG-FEM presented by Delcourte *et al.* (2009) to arbitrary interpolation orders and highly heterogeneous media in 2-D. The initial approach lies on the analytical integration of the mass and stiffness matrices on the reference element, implicitly assuming constant physical properties within each element of the mesh (Delcourte *et al.* 2009). Therefore, the construction of the numerical mesh to solve realistic problems in seismology becomes an extremely hard task [see for example Etienne *et al.* (2010) for the Volvi sedimentary basin and Wenk *et al.* (2013) for regional wave propagation]. In this work, we show that this restriction can be avoided by allowing changes in material properties inside the mesh elements. For this we propose a completely different approach from that proposed by Castro *et al.* (2010) which results in additional terms in the numerical scheme. Instead, we introduce another set of quadrature points for the material approximation and calculate the integrals by, precise enough, quadratures rules, thus avoiding strong modifications of the numerical scheme. We restrict to elastic heterogeneous media, though the method can be extended to anelastic and anisotropic elastic media provided the pseudo-conservative formulation is abandoned. The extension to 3-D media is straightforward and it will be published elsewhere.

The paper is structured as follows. After a brief introduction of the elastodynamic equations in Section 2, the numerical scheme is proposed, in Section 3, with emphasis on the pseudo-conservative formulation used by Delcourte *et al.* (2009) or Etienne *et al.* (2010). Then, the discrete problem is derived with two sets of nodes within the triangular elements for interpolation and numerical integration by appropriate quadrature rules. Numerical applications are presented in Section 4. To test the accuracy of the method, a classical *hp*-convergence study on smoothly varying media is performed. Next, we study the effect of a strong discontinuity in material properties within the triangular elements on the numerical simulations with respect to the accuracy of the quadrature rule. We end with an interesting example of a 2-D sedimentary basin with linear gradient velocity profile which illustrates the interest of this new method.

2 ELASTODYNAMIC EQUATIONS

We consider an isotropic, linearly elastic 2-D medium and solve the first-order hyperbolic system of elastodynamics (Virieux 1986),

$$\rho \partial_t \vec{V} = \nabla \cdot \overline{\overline{\sigma}},$$

$$\partial_t \overline{\overline{\sigma}} = \lambda (\nabla \cdot \vec{V}) \overline{\overline{I}} + \mu [\nabla \vec{V} + (\nabla \vec{V})^t], \tag{1}$$

where $\vec{V}$ and $\overline{\overline{\sigma}}$ are respectively the velocity vector and the stress tensor, $\overline{\overline{I}}$ is the identity matrix, ρ the density of the medium and λ and μ are the Lamé parameters. As the stress tensor is symmetric, let $\vec{W} = (\vec{V}, \vec{\sigma})^t$ contain the velocity vector $\vec{V} = (v_x, v_y)^t$ and the stress components $\vec{\sigma} = (\sigma_{xx}, \sigma_{yy}, \sigma_{xy})^t$, then, the system (1) can be rewritten in vector form as

$$\partial_t \vec{W} + A_x(\rho, \lambda, \mu)\, \partial_x \vec{W} + A_y(\rho, \lambda, \mu)\, \partial_y \vec{W} = 0, \tag{2}$$

with matrices A_x and A_y explicitly dependant on the medium parameters. The detailed expressions of these matrices can be found in Käser & Dumbser (2006) or Peyrusse *et al.* (2014).

Using this formulation, Käser & Dumbser (2006) derive a modal DG approach that has been extended for anisotropic (de la Puente *et al.* 2007) and viscoelastic media (Käser *et al.* 2007a). Castro *et al.* (2010) investigate the extension of the ADER-DG methodology to subcell resolution, allowing for variable material properties within the elements. This method uses the same basis functions

for the material expansion and, as a consequence, the variational formulation requires the calculation of additional terms and a new set of stiffness matrices to account for the spatial variation of the material properties. Contrary to the standard ADER-DG method, the stiffness matrices are now third-order tensors. To avoid computing and storing these extra terms, we choose a completely different approach. Following Benjemaa *et al.* (2007) and Delcourte *et al.* (2009), we introduce a change of variables on the stress components $\vec{\sigma} = (\sigma_{xx}, \sigma_{yy}, \sigma_{xy})^t \rightarrow \vec{\tilde{\sigma}}$, with

$$\vec{\tilde{\sigma}} = \left(\frac{1}{2}(\sigma_{xx} + \sigma_{yy}), \frac{1}{2}(\sigma_{xx} - \sigma_{yy}), \sigma_{xy} \right)^t , \tag{3}$$

which allows writing the system (2) in the pseudo-conservative form in the vector variable $\vec{\tilde{W}} = (\vec{V}, \vec{\tilde{\sigma}})^t$ as,

$$\Lambda(\rho, \lambda, \mu)\, \partial_t \vec{\tilde{W}} + \tilde{A}_x \partial_x \vec{\tilde{W}} + \tilde{A}_y \partial_y \vec{\tilde{W}} = 0 , \tag{4}$$

where the matrices $\tilde{A}_x$ and $\tilde{A}_y$ do not depend anymore on the material properties. But they are gathered in the diagonal matrix Λ given by,

$$\Lambda(\rho, \lambda, \mu) = \mathrm{diag}\left(\rho, \rho, \frac{1}{\lambda + \mu}, \frac{1}{\mu}, \frac{1}{\mu} \right). \tag{5}$$

To simplify notation, we will omit the $[\tilde{.}]$ notation on the transformed variables from hereon.

3 NUMERICAL SCHEME

We consider a bounded polyhedral domain $\Omega \in \mathbb{R}^2$ discretized by non-overlapping, conforming and straight-sided triangular elements T_e. Associated with the triangulation, let us consider the affine mapping $\mathcal{F}_e$ from an arbitrary triangular element T_e to the reference simplex $\triangle = \{(r, s): (r, s) > -1; r + s \leq 0\}$, and the approximation space $\mathbb{P}_p$, the finite dimensional subspace of polynomials of degree less or equal p defined on $\triangle$. Considering a basis of $\mathbb{P}_p$, $\{\Phi_j\}_{j=1}^N$, the piecewise polynomial approximation of $\vec{W}$ is defined locally on each element, through the affine mapping $\mathcal{F}_e$, as a linear combination of time-dependent fields,

$$\vec{W}_e(x, y, t) = \sum_{j=1}^{N} \vec{\hat{W}}_{ej}(t) \Phi_j [\mathcal{F}_e(x, y)] , \tag{6}$$

where $N = (p + 1)(p + 2)/2$ is the number of degrees of freedom in $\triangle$, that is the dimension of the approximation space $\mathbb{P}_p$.

As classical in the Galerkin method, the system (4) is multiplied by a test function $\Phi_r \in \mathbb{P}_p$ and integrated over each element T_e. Note that the introduction of non-constant material properties inside a triangle T_e is simply accounted by the calculation of a modified local mass matrix $\mathcal{M}_e$ term depending on the material properties,

$$\mathcal{M}_e\, \partial_t \vec{W}_e = \int_{T_e} \Phi_r^t\, \Lambda(\rho, \lambda, \mu)\, \partial_t \vec{W}_e \, \mathrm{d}\Omega . \tag{7}$$

The other terms in eq. (4), that is the ones containing spatial derivatives of the solution field and the fluxes between neighbouring elements, remain unchanged. The procedure avoids the calculation of additional terms but, in contrast, needs storing the inverse of $\mathcal{M}_e$, whose size is $N \times N$, for each element of the mesh and each component of Λ, three in number. This is done once during the simulation, in a pre-processing stage. Up to this point, the method is independent of the choice of the polynomial basis $\{\Phi_j\}_{j=1}^N$ in the expansion of eq. (6). We then adopt the nodal form of the DG-FEM (Hesthaven & Warburton 2008) based on a multidimensional lagrangian interpolation, centred fluxes and a second-order *leap-frog* time integration scheme. The reader is referred to Delcourte *et al.* (2009) for the complete construction of the numerical scheme. Note that the solution of system (4), where the matrices $\tilde{A}_x$ and $\tilde{A}_y$ do not depend on the material properties, is greatly simplified by the use of centred fluxes that do not require matrix diagonalization.

Three types of boundary conditions are applied: free-surface and absorbing boundary conditions which have already been detailed by Delcourte *et al.* (2009), and periodical boundary conditions that can be found in Peyrusse *et al.* (2014). The time step of a simulation is calculated using a formula slightly more restrictive as the standard one (Käser & Dumbser 2006) to account for the choice of non-equispaced interpolation nodes, as explained later in the document. From experiments, the time step writes

$$\Delta t = \min_{T_e} \Delta t_e \quad \Delta t_e = \frac{1}{3\, p} \frac{h_e}{v_{P|e}} , \tag{8}$$

where Δt_e is the local time step in the element T_e which depends on h_e, the smallest height of T_e, $v_{P|e}$ the maximum value of v_P in the element, and p the spatial interpolation degree.

3.1 Lagrangian interpolation

In the context of the FEM on simplicial meshes, the orthonormal basis of $\mathbb{P}_p$ known as the Dubiner–Koorwinder basis (Proriol 1957; Koorwinder 1975; Dubiner 1991) has interesting properties in terms of matrix conditioning and spectral accuracy (Owens 1998; Sherwin & Karniadakis 1995). Moreover, it is readily calculated by a Gram-Schmidt orthogonalization procedure, what leads to explicit formulas for high-order interpolation and derivation. Even if the orthogonality of the previous basis is attractive, the impact of using such spectral expansion in a DG-FEM is that all modes are needed to evaluate $\vec{W}_i$ pointwise, and therefore to calculate the fluxes between contiguous elements (Hesthaven & Warburton 2008).

Another possibility is to resort, like in classical FEM (Hesthaven & Teng 2000; Taylor *et al.* 2000; Warburton *et al.* 2000; Hesthaven & Warburton 2008), to a multidimensional lagrangian interpolation basis of $\mathbb{P}_p$, associated with an appropriate set of nodes (r_i, s_i), $i = 1, N$ defined inside and on the edges of the reference simplex, which satisfies $\Psi_k(r_i, s_i) = \delta_{ki}$ (cardinality condition). Then, we can also write eq. (6) in the standard triangle as

$$\vec{W}(r, s, t) = \sum_{j=1}^{N} \vec{\hat{W}}_j(t) \Phi_j(r, s) = \sum_{k=1}^{N} \vec{W}_k(t) \Psi_k(r, s). \tag{9}$$

Using the generalized Vandermonde matrix $V_{ij} = \Phi_j(r_i, s_i)$, i.e. the matrix whose columns are the Dubiner–Koorwinder basis evaluated at the set of points $\{(r_i, s_i)\}$, the relation between modal and nodal expansions reads,

$$\vec{W}_i(t) = \sum_{j=1}^{N} V_{ij} \vec{\hat{W}}_j(t) \quad \text{and} \quad \Psi_k(r, s) = \sum_{j=1}^{N} V_{kj}^{-T} \Phi_j(r, s). \tag{10}$$

The choice of the nodal set is crucial for a stable and efficient method. The reader is referred to Pasquetti & Rapetti (2010) for a compilation of different nodal sets with good interpolation and integration properties within the standard simplex. In a DG-FEM methodology, the choice appears less crucial than in classical SEM where the continuity between elements is required and the global mass matrix is preferably diagonal for an efficient application of explicit time-schemes (Mercerat *et al.* 2006). As stated by Pasquetti & Rapetti (2010) 'for reasonable values of polynomial order (less than 10), *simplicity* in the construction should prevail'. In the context

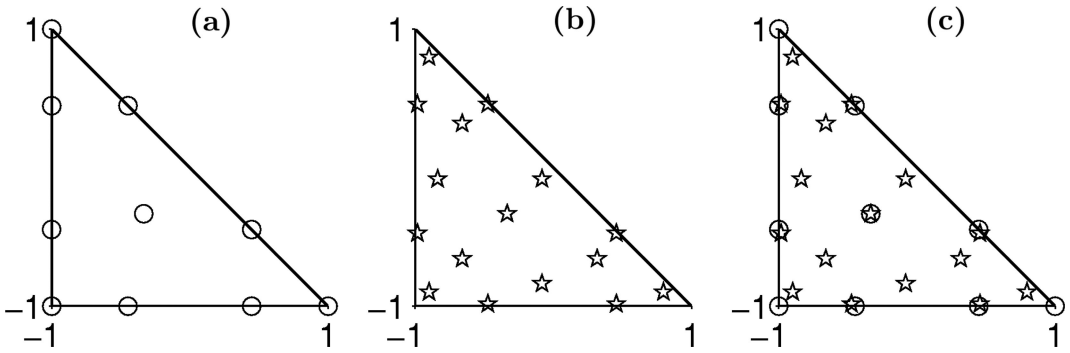

Figure 1. (a) Interpolation points in the standard triangle for $\mathbb{P}_3$. (b) Quadrature points in the standard triangle (Dunavant – order 8). (c) Both set of points plotted in the standard triangle.

Table 1. Dunavant formulas for the standard triangle and their accuracy order (i.e. maximum polynomial order that is exactly integrated by the quadrature rule).

Number of points	6	12	16	25	33	42
Order	4	6	8	10	12	14

of seismic wave modelling with the triangular spectral element method (TSEM), Mazzieri & Rapetti (2012) have recently shown that even equidistant interpolation nodes in the standard triangle perform satisfactorily (i.e. similar dispersion characteristics than other set of nodes) for moderate interpolation orders.

In this work, we adopt the set of nodes presented by Warburton (2006) and coined 'warp & blend'. Their calculation is straightforward and they present excellent properties in $\triangle$ for high-order interpolation. The nodal set for $\mathbb{P}_3$ is shown in Fig. 1(a).

3.2 Mass matrix calculation

In order to calculate the local mass matrix expressed by eq. (7), we make use of Gauss-type quadrature rules within the standard triangle published by Dunavant (1985). The quadrature points need not to coincide with the nodal set used for interpolation, and they are generally more than N to acquire enough precision (see next section). We use here the Dunavant (1985) sets whose properties are summarized in Table 1. An example of a degree 8 rule of 16 points, that is a rule that integrates exactly a polynomial of degree 8, is shown in Fig. 1(b). For the edge integrals related to flux calculations, uni-dimensional Gauss points can be used along each edge.

Let define $V^*_{ij} = \Phi_j(\xi_i, \eta_i)$ with $\{(\xi_i, \eta_i)\}$ the chosen N_q quadrature points ($N_q > N$). Then, we use the lagrangian expansions of the test function Ψ_r, the solution vector $\vec{W}_e$ and $c(r, s)$ for the material property in eq. (5). After transformation to $\triangle$, the integral in eq. (7) reads

$$\mathcal{M}_e\, \partial_t \vec{W}_e = J_e \int_{\triangle} \Psi_r(r,s)^T\, c(r,s)\, \partial_t \vec{W}(r,s)\, \mathrm{d}r\, \mathrm{d}s,$$

$$\approx J_e \sum_{q=1}^{N_q} \omega_q \left[\Psi_r(\xi_q,\eta_q)^T\, c(\xi_q,\eta_q) \sum_{j=1}^{N} \partial_t \vec{W}_j\, \Psi_j(\xi_q,\eta_q) \right]$$

$$= J_e \sum_{q=1}^{N_q} \omega_q \left(\sum_{k=1}^{N} V^{-1}_{rk} \Phi_k(\xi_q,\eta_q) \right)^T c(\xi_q,\eta_q)$$

$$\sum_{j=1}^{N} \partial_t \vec{W}_j \left(\sum_{k=1}^{N} V^{-1}_{jk} \Phi_k(\xi_q,\eta_q) \right). \qquad (11)$$

The rj-component of the local mass matrix is then given by

$$(\mathcal{M}_e)_{rj} = J_e \sum_{q=1}^{N_q} \boldsymbol{H}^T_{qr}\, \omega_q c(\xi_q,\eta_q)\, \boldsymbol{H}_{jq} \qquad (12)$$

with ω_q the quadrature weights, J_e the (constant) jacobian of the affine transformation, and $\boldsymbol{H} = \boldsymbol{V}^{-T} \boldsymbol{V}^{*T}$ a rectangular matrix of dimension $N \times N_q$. In matrix form, the local mass matrix reads $\mathcal{M}_e = \boldsymbol{H} \boldsymbol{\Omega}_e \boldsymbol{H}^T$, with $\boldsymbol{\Omega}_e = J_e\, \mathrm{diag}[\omega_q\, c(\xi_q, \eta_q)]$ the $N_q \times N_q$ diagonal matrix containing the product of the quadrature weight and the material property (e.g. density or inverse of Lame's constants) as defined by eq. (5) evaluated at each quadrature point.

In the case of constant material properties within an element, the integrals are calculated analytically using the generalized Vandermonde matrix (i.e. no quadrature rule is needed) and scaled by the product of the Jacobian and the material property of each element (Mercerat *et al.* 2006; Pasquetti & Rapetti 2006). We recall that the elementary mass matrices corresponding to each material constant have dimension $N \times N$. Therefore, they are easily inverted in a pre-processing stage before simulation starts for each element of the mesh. At each time step, they are applied to solve the system of equations (4).

4 NUMERICAL EXAMPLES

4.1 *hp*-Convergence study

In this section, we propose a first verification of the method when applied to smoothly varying materials. For this, we perform a numerical convergence study which consists in measuring the error between the numerical solution and a reference exact solution of the problem, for a series of refined meshes and different polynomial approximations. In a preliminary step, it seems interesting to us to recall the intrinsic properties of the high-order DG method based on centred fluxes and a leap-frog time integration scheme by considering an homogeneous medium. Thereafter, the new DG extension is applied to a heterogeneous medium following the approach proposed by Castro *et al.* (2010).

We consider the propagation of plane sinusoidal P and S waves along the diagonal direction $\vec{n} = (1, 1)^t$. The computation domain is the square $[-1, 1] \times [-1, 1]$ and periodicity conditions are applied at its boundaries. The exact plane wave is defined by

$$\vec{W}^{ex}(x, y, t) = \vec{R}_S\, S_S + \vec{R}_P\, S_P\,, \qquad (13)$$

where

$$S_S = \sin(\vec{k} \cdot \vec{X} + v_S\, \|\vec{k}\|\, t)\,, \quad S_P = \sin(\vec{k} \cdot \vec{X} - v_P\, \|\vec{k}\|\, t)\,, \qquad (14)$$

$\vec{k} = (2\pi,\ 2\pi)^t$ is the wavenumber and $\vec{X} = (x,\ y)^t$. According to the change of variables (3) and the corresponding set of unknowns, the vectors $\vec{R}_S$ and $\vec{R}_P$ write, respectively

$$\vec{R}_S = \left(\frac{\sqrt{2}}{2}\, v_S,\ -\frac{\sqrt{2}}{2}\, v_S,\ 0,\ \mu,\ 0 \right)^t \quad \text{and}$$

$$\vec{R}_P = \left(\frac{\sqrt{2}}{2}\, v_P,\ \frac{\sqrt{2}}{2}\, v_P,\ -(\lambda + 2\mu),\ 0,\ -\mu \right)^t . \tag{15}$$

For the first application, the material properties are set constant and equal to $\rho = 1$ kg m^{-3}, $\lambda = 2$ kg m^{-1} s^2 and $\mu = 1$ kg m^{-1} s^2 implying that $v_P = 2$ m s^{-1} and $v_S = 1$ m s^{-1}. It can easily be checked that $\vec{W}^{ex}$ is solution of the pseudo-conservative system (4). Initialization of the leap-frog scheme requires evaluating the velocity components at time $t = 0$ and the stress components at $t = \frac{\Delta t}{2}$ thanks to (13). Simulations are performed until time $t_{\text{end}} = 2\sqrt{2}$ s, insuring that P and S waves have travelled one and two wavelengths, respectively. Series of uniform meshes with different refinement levels have been constructed by dividing the domain in square cells which are split in two triangles, as illustrated in the example of Fig. 3. The mesh length h refers to the smallest edge (or height) of the corresponding discretization. In order to cover a wide range of values for h but avoid making too many calculations, h is chosen so that $1/h$ is a multiple of 4. For each mesh, we calculate a global L^2-error that covers the entire computational domain and for all components, at t_{end}, between $\vec{W}^{ex}$ and the solution of the numerical scheme. At time $t = n\,\Delta t$, this error writes

$$err^n_{L^2} = \left[\sum_{i=1}^{N_T} \int_{T_i} \left\{ \sum_{j=1}^{2} \left(W^{ex}_j(x, y, n\,\Delta t) - W^n_{j,i} \right)^2 + \sum_{j=3}^{5} \left(W^{ex}_j\left(x, y, \left(n+\frac{1}{2}\right)\Delta t\right) - W^{n+1/2}_{j,i} \right)^2 \right\} \mathrm{d}\Omega \right]^{1/2}, \tag{16}$$

where the index j refers to components of $\vec{W}$ and $W_{j,i}$ represents the computed value of the jth component of $\vec{W}$ in the element T_i.

Different polynomials orders have been used, from hereon the notation $\mathcal{P}_p$ refers to the DG method based on a polynomial approximation of degree p. We present, in Fig. 2(a), the L^2-error at t_{end} with respect to the mesh size h for polynomial degrees p ranging from 1 to 5. The figure proves a second-order convergence of the DG method, whatever the value of $p \geq 2$, even if the error levels are much lower as the polynomial order of the spatial approximation increases. Delcourte & Glinsky (2015) proved that the theoretical order of convergence is $\mathcal{O}(\Delta t^2 + h^p) = \mathcal{O}(\alpha^2 h^2 + h^p)$ [from eq. (8), Δt is proportional to h, i.e. $\Delta t = \alpha\, h$] which implies that, except for $p = 1$ for which a first-order convergence is expected, the global convergence rate is dominated by the time discretization. Table 2 contains the values of the L^2-error for some mesh sizes and the corresponding convergence orders, defined by

$$\mathcal{O}_{L^2}(h_i) = \frac{\log[err_{L^2}(h_{i+1})/err_{L^2}(h_i)]}{\log(h_{i+1}/h_i)},$$

which confirms the expected convergence results. Note that the DG $\mathcal{P}_1$ method produces slightly better results than the theory for this case, probably thanks to the time scheme which is second-order accurate. A way to improve the convergence results is to remove the limitation due to the time-scheme by using higher (even)-order leap-frog schemes as proposed by Young (2001) and applied to elastodynamic equations by Delcourte & Glinsky (2015). In this paper, we limit ourselves to the standard 2nd order leap-frog method and keep the extension to higher-order time schemes for a further study. Despite the limitation due to the temporal approximation, the methods based on high-order spatial discretizations allow a noticeable error reduction, and we will emphasize their interest in the remainder of this paper.

To focus on the properties of the spatial discretization method, we reproduce this convergence study by fixing for each $\mathcal{P}_p$ method the time step to a very small value Δt_p, the same for all mesh sizes h, forcing the error to mainly depend on the spatial discretization. For each polynomial order, this time step is set to the value from eq. (8) corresponding to a 'fictitious' $h_p = 2.0 \times 10^{-3}$ m, ensuring comparable conditions for each interpolation order. The values of Δt_p can be found in Table 3. Here we limit ourselves to smaller values for $1/h$, simply for reasons of computing time. The corresponding convergence curves are presented in Fig. 2(b). We clearly notice that, once the influence of the second-order time discretization is reduced, the convergence increases with the degree of the polynomial interpolation. Moreover, we prove the correctness of the spatial discretization since the expected convergence in $\mathcal{O}(\Delta t_p^2 + h^p) = \mathcal{O}(\alpha^2\, h_p^2 + h^p) \simeq \mathcal{O}(h^p)$ (since $h_p \ll h$) is achieved as confirmed by the convergence orders of Table 3. We notice that, for even values of p, the convergence rate is better than expected, that is the convergence order is closer to $p + 1$ than to p. Such behaviour is observed for other systems, for instance for Maxwell's equations, when central fluxes are used, as explained by Hesthaven & Warburton (2008) referring to an even-odd pattern. Note that for all other numerical applications presented in this paper, the optimal time step is used in order to minimize the computation time.

Now in a second stage, we test the new methodology for a smoothly varying medium defined by $\lambda(x, y) = 2 + 0.5 \sin(2\pi x + 2\pi y)$, ρ and μ keeping the same constant values as for the homogeneous case. We choose to introduce variations only on λ, unlike Castro *et al.* (2010) which also include similar sinusoidal perturbations for ρ and μ, without loosing the interest and complexity of the test-case. In both studies, v_S remains constant equal to 1 m s^{-1} but our assumption greatly simplifies the calculation of the additional terms, as we shall see in the following. We then have $v_P = [4 + 0.5 \sin(2\pi x + 2\pi y)]^{1/2}$ whose variations are plotted in the square domain in Fig. 3. We follow exactly the same approach for the convergence study, except that, in order to ensure that $\vec{W}^{ex}$ is still an exact solution of the heterogeneous problem, we need to add corrective source terms to the pseudo-conservative system. These corrective terms, detailed in Appendix A, depend on the spatial derivatives of λ and v_P. To include these terms in a manner which is consistent with the leap-frog time scheme, the components corresponding to velocity equations (respectively stress equations) are taken at an intermediate time, that is at $(n + 1/2)\Delta t$ [respectively $(n + 1)\Delta t$].

Different quadrature formulas can be used to account for the intra-element material variations. In a first trial, the material properties are approximated by second-degree polynomials. Therefore, for a polynomial interpolation of degree p, we choose a quadrature formula of order $2p + 2$ for the calculation of the modified mass matrices.

We present, in Fig. 4, the L^2-error at t_{end} with respect to the mesh size h, for values of p from 1 to 5. We notice that the results are relatively different from the homogeneous case for which a second-order convergence is obtained for all values of p. By studying more

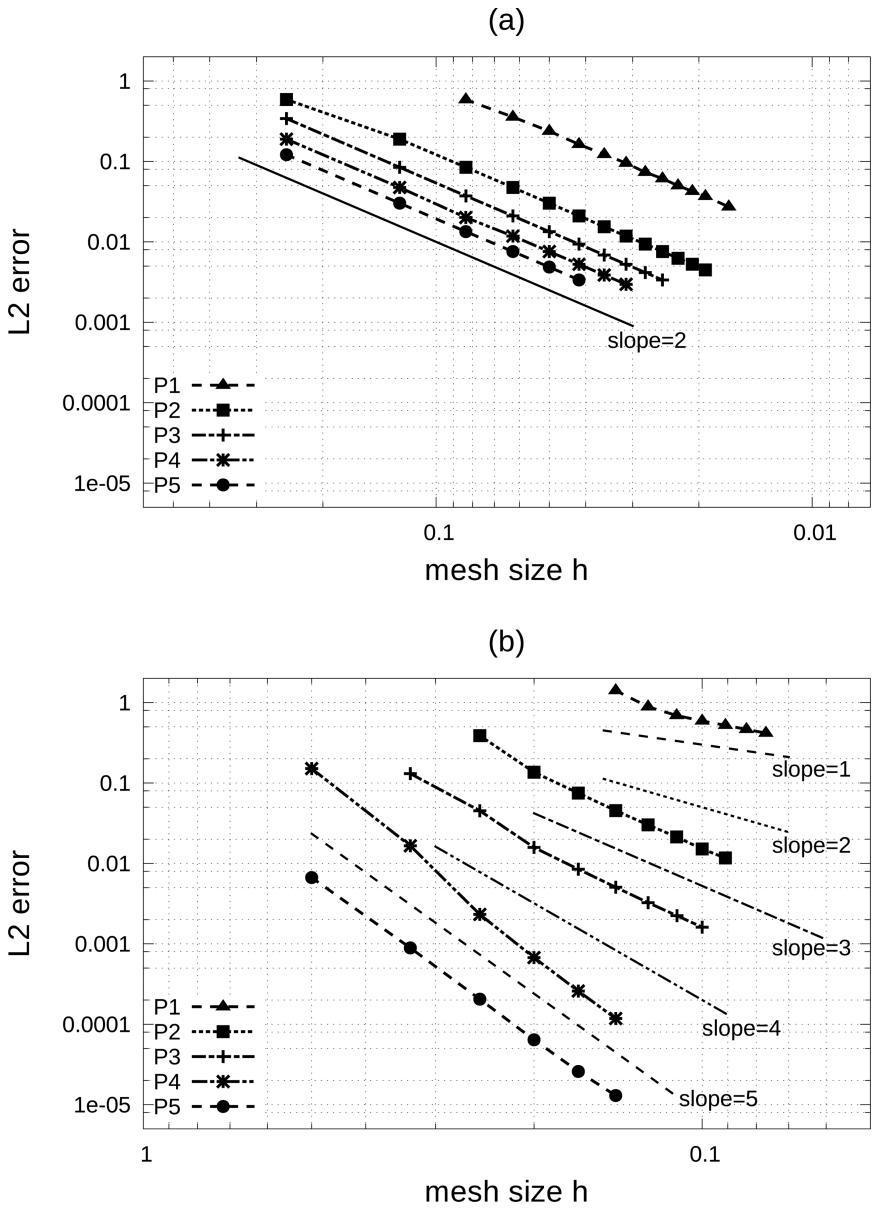

Figure 2. Convergence study for a homogeneous medium: error as a function of the mesh spacing h for different methods $\mathcal{P}_p$ (a) using the optimal time step determined by the condition (8), (b) with a fixed tiny time step Δt_p in order to appreciate the convergence of the spatial integration.

Table 2. Results for the *hp*-convergence study; case of a homogeneous medium. Global error of eq. (16) as a function of h for the DG $\mathcal{P}_p$ method. Optimal Δt from the condition (8).

	$\mathcal{P}_1$			$\mathcal{P}_2$		$\mathcal{P}_3$		$\mathcal{P}_4$		$\mathcal{P}_5$	
$1/h$	err_{L^2}	$\mathcal{O}_{L^2}$	$1/h$	err_{L^2}	$\mathcal{O}_{L^2}$	err_{L^2}	$\mathcal{O}_{L^2}$	err_{L^2}	$\mathcal{O}_{L^2}$	err_{L^2}	$\mathcal{O}_{L^2}$
12	5.87×10^{-1}	–	4	5.89×10^{-1}	–	3.41×10^{-1}	–	1.89×10^{-1}	–	1.21×10^{-1}	–
16	3.57×10^{-1}	1.72	8	1.89×10^{-1}	1.63	8.43×10^{-2}	2.01	4.74×10^{-2}	1.99	3.03×10^{-2}	1.99
20	2.38×10^{-1}	1.81	12	8.44×10^{-2}	1.98	3.72×10^{-2}	2.01	2.10×10^{-2}	2.00	1.34×10^{-2}	2.01
24	1.63×10^{-1}	2.07	16	4.74×10^{-2}	2.00	2.10×10^{-2}	1.98	1.18×10^{-2}	2.00	7.58×10^{-3}	1.98
28	1.22×10^{-1}	1.87	20	3.03×10^{-2}	2.00	1.34×10^{-2}	2.01	7.58×10^{-3}	1.98	4.85×10^{-3}	2.00
32	9.54×10^{-2}	1.84	24	2.10×10^{-2}	2.00	9.36×10^{-3}	1.96	5.26×10^{-3}	2.00	3.36×10^{-3}	2.01

precisely the error values in Table 4, we observe much higher error values for the coarser meshes, which gives the illusion of a better convergence. If we except the few highest values of h, the error levels of the methods $\mathcal{P}_p$ with $p \geq 2$ are comparable (even slightly lower) than for the homogeneous case. For $p = 4$ and 5, the convergence order quickly reaches values equal to 2. For $p = 2$ and 3, the value of $\mathcal{O}_{L^2}$ decreases more slowly from values between 3 and 4 but second-order convergence will probably be reached when h continues to

Table 3. Results for the *hp*-convergence study for the homogeneous medium. Global error (16) as a function of h for the DG $\mathcal{P}_p$ method. Influence of the spatial discretization, time step set constant to a very small value $\Delta t_p = \alpha h_p$.

Δt (s)	$\mathcal{P}_1$ 2.34×10^{-4}			$\mathcal{P}_2$ 1.17×10^{-4}		$\mathcal{P}_3$ 7.84×10^{-5}		$\mathcal{P}_4$ 5.88×10^{-5}		$\mathcal{P}_5$ 4.71×10^{-5}	
$1/h$	err_{L^2}	$\mathcal{O}_{L^2}$	$1/h$	err_{L^2}	$\mathcal{O}_{L^2}$	err_{L^2}	$\mathcal{O}_{L^2}$	err_{L^2}	$\mathcal{O}_{L^2}$	err_{L^2}	$\mathcal{O}_{L^2}$
8	8.87×10^{-1}	–	3	–	–	1.31×10^{-1}	2.23	1.66×10^{-2}	5.43	8.90×10^{-4}	4.96
9	6.92×10^{-1}	2.09	4	3.88×10^{-1}	–	4.51×10^{-2}	3.70	2.32×10^{-3}	6.86	2.05×10^{-4}	5.10
10	5.90×10^{-1}	1.52	5	1.36×10^{-1}	4.69	1.58×10^{-2}	5.52	6.76×10^{-4}	5.52	6.41×10^{-5}	5.20
11	5.21×10^{-1}	1.30	6	7.48×10^{-2}	3.27	8.48×10^{-3}	3.41	2.59×10^{-4}	5.25	2.59×10^{-5}	4.96
12	4.64×10^{-1}	1.33	7	4.53×10^{-2}	3.26	5.06×10^{-3}	3.34	1.18×10^{-4}	5.11	1.30×10^{-5}	4.47
13	4.16×10^{-1}	1.36	8	3.01×10^{-2}	3.06	3.25×10^{-3}	3.31	–	–	–	–

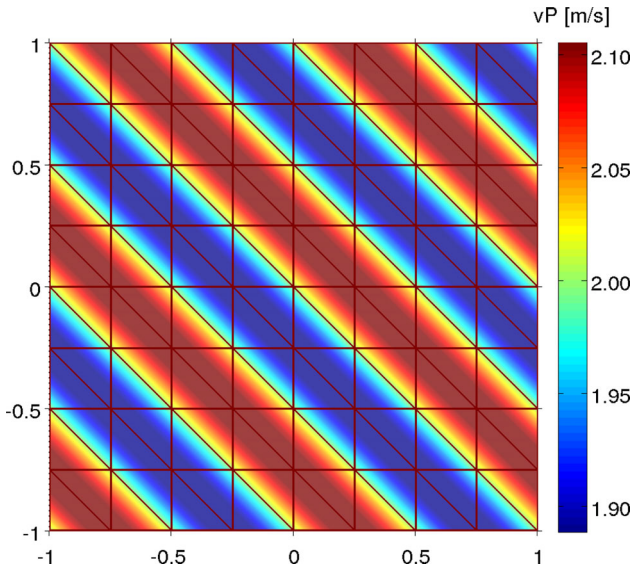

Figure 3. Example of uniform triangular mesh ($1/h = 4$) over the smoothly varying velocity model used in the *hp*-convergence test.

decrease. For $p = 1$, a first-order convergence is obtained which is consistent with the theoretical value, but slightly less than for the homogeneous case. This can be explained by the discretization of the corrective terms for this case, which are simply calculated at the three interpolation nodes of $\mathcal{P}_1$ following the procedure described in Appendix A. Note however that we are mainly interested in the convergence of high-order methods.

Finally, to investigate the impact of the order of the quadrature formula, this convergence study has also been made considering two other sets of quadrature points: the first one corresponding to an integration of the modified mass matrix exact until order $2p$ (i.e. no order left for the material variations), and a second one for which this integration is exact until order $2p + 4$ (i.e. order 4 for the material variations). The convergence results are almost exactly the same and do not depend on the order of the quadrature formula used for the calculation of the modified mass matrices. This proves that it would be enough to use a formula of order $2p$ to take into account a smooth variation in properties within the elements (i.e. gradient models). This is in accordance to classical SEM in quadrangles where the Gauss–Lobatto–Legendre quadrature rule exactly integrates polynomials of order $2p - 1$ with $p + 1$ points (Canuto *et al.* 1988), that is leaving no extra degree for intra-element material variations. As we shall see in the next section, this may not be the case when the variations in properties are not smooth within the elements.

As a final remark, we stress that the choice of different sets of quadrature points has no influence on the CPU time of the simulation. Since the modified mass matrices, of size $N \times N$ are calculated, inverted and stored for each triangle of the mesh, only once in a pre-processing stage, the additional cost due to a higher

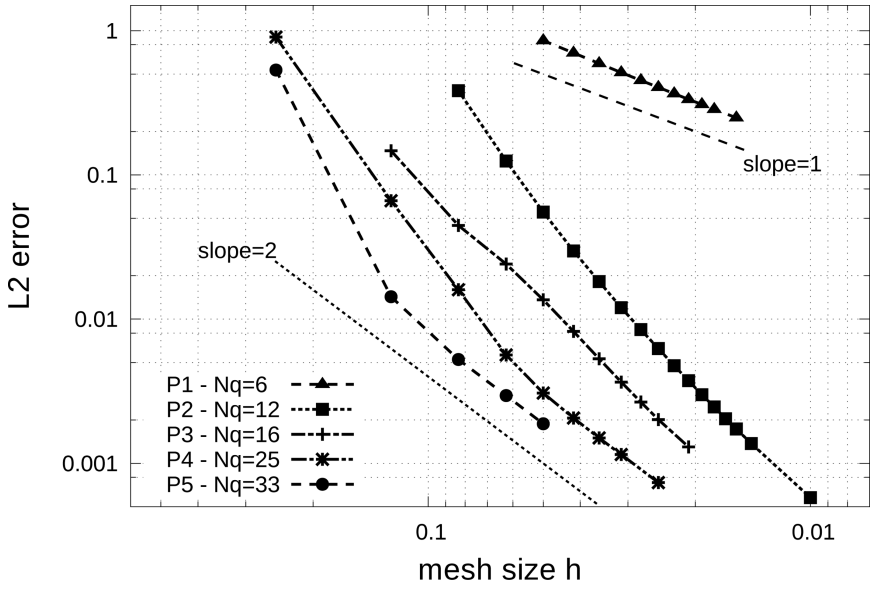

Figure 4. Convergence study for a smoothly varying heterogeneous medium: error as a function of the mesh spacing h for different methods $\mathcal{P}_p$.

Table 4. Numerical convergence results for the DG $\mathcal{P}_p$ methods for the smoothly varying heterogeneous medium.

	$\mathcal{P}_1$			$\mathcal{P}_2$			$\mathcal{P}_3$		$\mathcal{P}_4$		$\mathcal{P}_5$	
$1/h$	err_{L^2}	$\mathcal{O}_{L^2}$	$1/h$	err_{L^2}	$\mathcal{O}_{L^2}$	$1/h$	err_{L^2}	$\mathcal{O}_{L^2}$	err_{L^2}	$\mathcal{O}_{L^2}$	err_{L^2}	$\mathcal{O}_{L^2}$
20	8.54×10^{-1}	–	12	3.84^{-1}	–	4	–	–	9.04^{-1}	–	5.34×10^{-1}	–
24	7.01×10^{-1}	1.08	16	1.25^{-1}	3.90	8	1.47×10^{-1}	–	6.63^{-2}	3.76	1.43×10^{-2}	5.22
28	5.93×10^{-1}	1.08	20	5.52^{-2}	3.66	12	4.46×10^{-2}	2.94	1.60^{-2}	3.50	5.25×10^{-3}	2.47
32	5.13×10^{-1}	1.08	24	2.97^{-2}	3.39	16	2.41×10^{-2}	2.13	5.64^{-3}	3.62	2.95×10^{-3}	2.00
36	4.52×10^{-1}	1.07	28	1.82^{-2}	3.17	20	1.36×10^{-2}	2.56	3.07^{-3}	2.72	1.88×10^{-3}	2.01
40	4.05×10^{-1}	1.04	32	1.20^{-2}	3.12	24	8.20×10^{-3}	2.77	2.06^{-3}	2.18	–	–

number of quadrature points is negligible compared to the total computational time of the simulation. We come back to this point in the next section.

4.2 Amplification due to a surface layer

A classical problem in ground motion studies is the reliable evaluation of the lithological site effect, that is the amplification of seismic motion caused by the soil layers near the ground surface (Bard & Bouchon 1985). These layers are generally composed of soft materials with extremely low and highly variable shear wave velocities (less than 100 m s^{-1} in some cases). This constitutes the main bottleneck for regional numerical simulations of ground motion as the size of elements (or the grid size for a finite difference method) must be small enough to accurately account for the minimum propagated wavelenghts (e.g. tens of metres) and the strong heterogeneity of the medium.

We study in this section the amplification due to a superficial layer of 40-m-thick overlying a half-space. The material properties are shown in Table 5, where we note the high impedance contrast between both media (with a velocity ratio greater than 6).

Since this problem is 1-D but studied in two dimensions of space, the computational domain is 3000 m deep and of variable width $2\,h$ where h is the mesh size. Uniform triangular meshes are constructed by considering 3 points in the x-direction whatever the value of h. Periodicity conditions are applied in the lateral boundaries of the domain, a free-surface condition at the top and absorbing conditions at the bottom. The incoming plane wave has a SV polarization and a Ricker source time function with central frequency of 2 Hz corresponding to a maximum frequency around $f_{\max} = 6$ Hz. Then, the minimum wavelength in the surface layer is $v_S/f_{\max} = 25$ m. The incident wave is introduced in the bedrock part of the model through a right-hand side of the horizontal component v_x following the method detailed in Peyrusse *et al.* (2014).

Table 5. Physical parameters for the soft layer problem overlying a bedrock.

		Half-space	Soft layer
S-wave velocity	(m s^{-1})	1000	150
P-wave velocity	(m s^{-1})	2450	365
Density	(kg m^{-3})	2100	1800

According to theory (Kramer 1996), resonant peaks at $f_n = (2n - 1)v_S/4H = (2n - 1)\,0.9375$ Hz, $n \in \mathbb{N}$, are expected and three of them, respectively at 0.9375, 2.8125 and 4.6875 Hz, are in the frequency range of interest. Besides, the amplitude of the amplification is determined by the impedance contrast between the soft layer and the half-space which, in this case, is equal to $a = 2\,(\rho\, v_S)_{\text{half-space}}/(\rho\, v_S)_{\text{layer}} = 4.2 \times 10^6/2.7 \times 10^5 \simeq 15.5555$.

Several combinations of uniform triangular meshes and quadrature/interpolation points are used in order to illustrate the interest of high-order methods and the improvements brought by the new DG formulation. First, we consider a series of meshes honouring the interface between the media. Then, the mesh size h must be a divisor of the soft layer depth that is $h \in \{5, 10, 20, 40\}$. We are interested in the transfer functions (i.e. spectral ratio between the waveform recorded at the free-surface and the incident waveform) of the horizontal velocity component v_x and compare the results to the theoretical values of amplication and associated frequencies in the frequency range [0, 6] Hz. Time simulations are run until $t = 16$ s, all spectra and spectral ratios are calculated with a frequency step $\Delta f = 2.5 \times 10^{-3}$ Hz. The solutions corresponding to $\mathcal{P}_2$, $\mathcal{P}_3$ and $\mathcal{P}_4$ methods are presented in Table 6. Here, since the medium do not vary inside the elements, the number of quadrature points has no importance as soon as the integration of the mass matrix is exact until order $2\,p$. For each method, we choose the 'optimal' result, that is (1) the one corresponding to the maximum value of h for a better efficiency and (2) for which the relative errors to the theoretical amplification and frequencies are at most 0.5 per cent.

Optimal solutions are obtained using $h = 5$ m for the $\mathcal{P}_2$ method, $h = 10$ m for the $\mathcal{P}_3$ method and $h = 20$ m with the $\mathcal{P}_4$ method. When comparing the CPU times of these three simulations, we notice that the high-order simulations are definitely more efficient. Note that, considering the sampling Δf, the frequencies of the first two peaks are exactly equal to the expected values for the three methods, the relative errors are then equal to zero. The maximum error on the amplitude is 0.3 per cent. The most accurate solution is obtained with the $\mathcal{P}_4$ method and $h = 20$ m, and it is taken as the reference in the following. The corresponding transfer function is compared to the theoretical values at the peaks (in solid lines) in Fig. 5 and the results are in perfect accordance. This proves the ability of the proposed DG method to accurately take into account strong contrasts in material properties.

Table 6. Accuracy of the $\mathcal{P}_p$ DG methods ($2 \le p \le 4$) for transfer functions when the mesh honours the discontinuity between the media. Values of amplification $a(i)$, corresponding frequency $f(i)$ (in Hz) for $i = 1, \ldots, 3$ and relative errors (in per cent) with respect to the theoretical values.

	h (m)	N_T	CPU (s)	$a(1)$	$err_a(1)$ (per cent)	$f(1)$ (Hz)	$err_f(1)$ (per cent)	$a(2)$	$err_a(2)$ (per cent)	$f(2)$ (Hz)	$err_f(2)$ (per cent)	$a(3)$	$err_a(3)$ (per cent)	$f(3)$ (Hz)	$err_f(3)$ (per cent)
$\mathcal{P}_2$	5	2400	572	15.5340	0.1	0.9375	0.0	15.5413	0.1	2.8125	0.0	15.5388	0.1	4.6900	0.05
$\mathcal{P}_3$	10	1200	455	15.5338	0.1	0.9375	0.0	15.5270	0.2	2.8125	0.0	15.5085	0.3	4.6900	0.05
$\mathcal{P}_4$	20	600	326	15.5336	0.1	0.9375	0.0	15.5336	0.1	2.8125	0.0	15.5540	0.01	4.6900	0.05

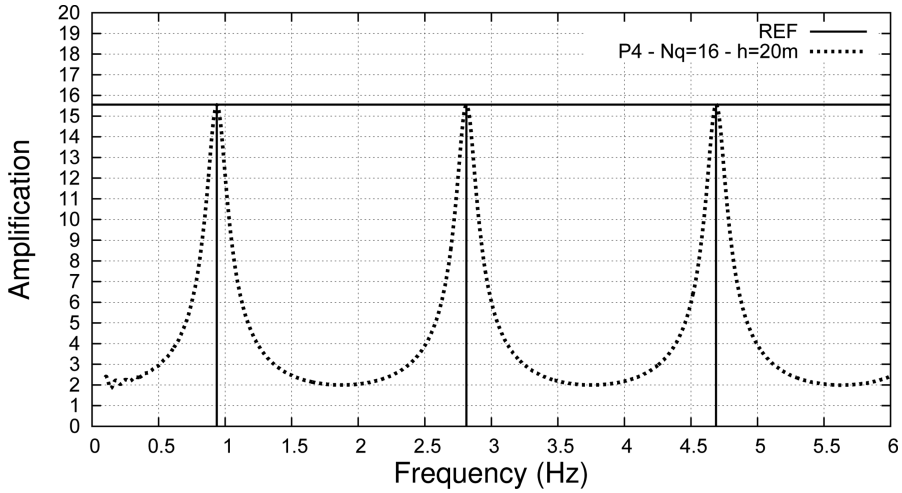

Figure 5. Transfer function of the horizontal velocity v_x at the surface. Results for the $\mathcal{P}_4$ DG method for $h = 20$ m, the mesh honours the interface between media.

In a second stage, we apply the new DG formulation to a mesh with the only constraint to satisfy the sampling of the minimum wavelength *without* honouring the interface between the media. We study the results of the $\mathcal{P}_4$ method and the mesh corresponding to $h = 25$ m which is the minimimum wavelength propagated in the soft layer. Four sets of quadrature points have been used ($N_q \in \{16, 25, 33, 42\}$) for which integration of the modified mass matrix is exact until orders 8, 10, 12 and 14, respectively.

We present, in Fig. 6, the transfer functions of the horizontal velocity v_x at the surface for the four sets of quadrature points. As previously, these solutions are compared to the theoretical values and are completed by relatives errors at the three peaks, given in Table 7. We first conclude that the solution corresponding to $N_q = 16$ is of poor quality: the first peak is not too badly approximated, but the frequencies associated to the two last peaks are overestimated, with relative errors about 3 per cent. The two following solutions, obtained using $N_q = 25$ and 33, are better and a clear improvement is visible for the two first peaks. For the last peak, the amplification is too high with $N_q = 25$ and the frequency is overestimated with $N_q = 33$ (both relative errors are about 2 per cent). None of these solutions are considered as acceptable following our accuracy criteria. Finally, the solution obtained with $N_q = 42$ is correct. The three peaks are well captured and all relative errors (on amplitude and frequency) are lower or equal to 0.5 per cent. This result proves that, by increasing the number of quadrature points and thus the accuracy of the modified mass matrices calculation, it is possible to converge towards the same solution as the initial DG method, but without the constraint of including the interface between media in the mesh.

To complete these transfer functions, we present in Fig. 7 the time evolution of the horizontal velocity for the less and the most accurate cases. These solutions are compared to the reference solution, here the value obtained using the $\mathcal{P}_4$ method and the mesh size $h = 20$ m. First, the solution obtained using $N_q = 16$ quadrature points (Fig. 7a) is too imprecise. After the first reflection of the incident wave at the surface, we notice a net delay (for times greater than 2.5 s) in comparison to the reference solution which results from an insufficient approximation of the strong jump in the material properties. If a smoothly varying material can be accurately taken into account without any additional quadrature points compared to the homogeneous case (as seen in the previous section), it is clear that a strong discontinuity of the material properties needs more accurate quadrature formulas. A clear improvement appears in the solution corresponding to $N_q = 42$ (order 14). The result of the new DG method is similar to the reference one, for the entire signal duration.

Contrary to the results presented by Castro *et al.* (2010) for a intra-element material discontinuity, we did not encounter any oscillation when increasing the number of quadrature points. For the various tests we performed, the use of more accurate quadrature formulas for the calculation of the modified mass matrices generally leads to improved solutions. The only limitation of this method comes from the quadrature formulas themselves which are exact for polynomial functions. It would be interesting to look for more general integration formulas, applicable to other types of functions.

Table 7 also presents the CPU times of the simulations. These times are similar for the four values of N_q which proves that the number of quadrature points used for the calculation of the modified mass matrix has no effect on the total CPU time of the simulation. Then, we stress that the achieved accuracy has no extra cost. Moreover, the use of this mesh ($h = 25$ m) allows a reduction of the CPU time of 30 per cent compared to the reference solution ($\mathcal{P}_4$ method, $h = 20$ m) associated to the initial method based on meshes honouring the interface between media.

This test confirms that the high-order DG method produces acceptable solutions using four to five interpolation nodes per minimum wavelength. Similar results are found for other high-order methods applied to elastic wave propagation (De Basabe *et al.* 2008; Seriani & Oliveira 2008; Liu *et al.* 2012). The new methodology, which allows material variations inside elements, significantly reduces the constraint during mesh generation. The only condition to be satisfied concerns the sampling of the minimum propagated wavelength. Moreover, this example proves that the method is sufficiently robust to deal with strong jumps on the material properties. Contrary to the previous case of a smooth velocity model, high-order quadrature formulas are necessary to better sample the strong velocity contrast and produce accurate solutions.

One of the main advantages is that, removing the constraint on interfaces, the meshes contain less elements, the global time step is generally increased and this results in a reduction in CPU time. For this 1-D test case (i.e. refinement made in only one direction) the gain in CPU time is of the order of 30 per cent. Comparable

or even better results are to be expected for 2-D and 3-D mesh configurations.

4.3 2-D sedimentary basin

We now turn to a more complex example of a 2-D sedimentary basin with variable seismic velocities lying on an homogeneous substratum. This geometry is prone to generate high seismic amplifications and long-lasting seismograms because of trapped surface waves inside the basin. An extensive study of the seismic response of such alluvial basins is beyond the scope of this paper and the interested reader can be referred to classical works such as Bard & Bouchon (1980a,b) and Sánchez-Sesma & Luzón (1995). The main interest here is to illustrate the geometrical flexibility and the enhanced mesh adaptativity provided by the use of an unstructured triangulation with non-constant material properties.

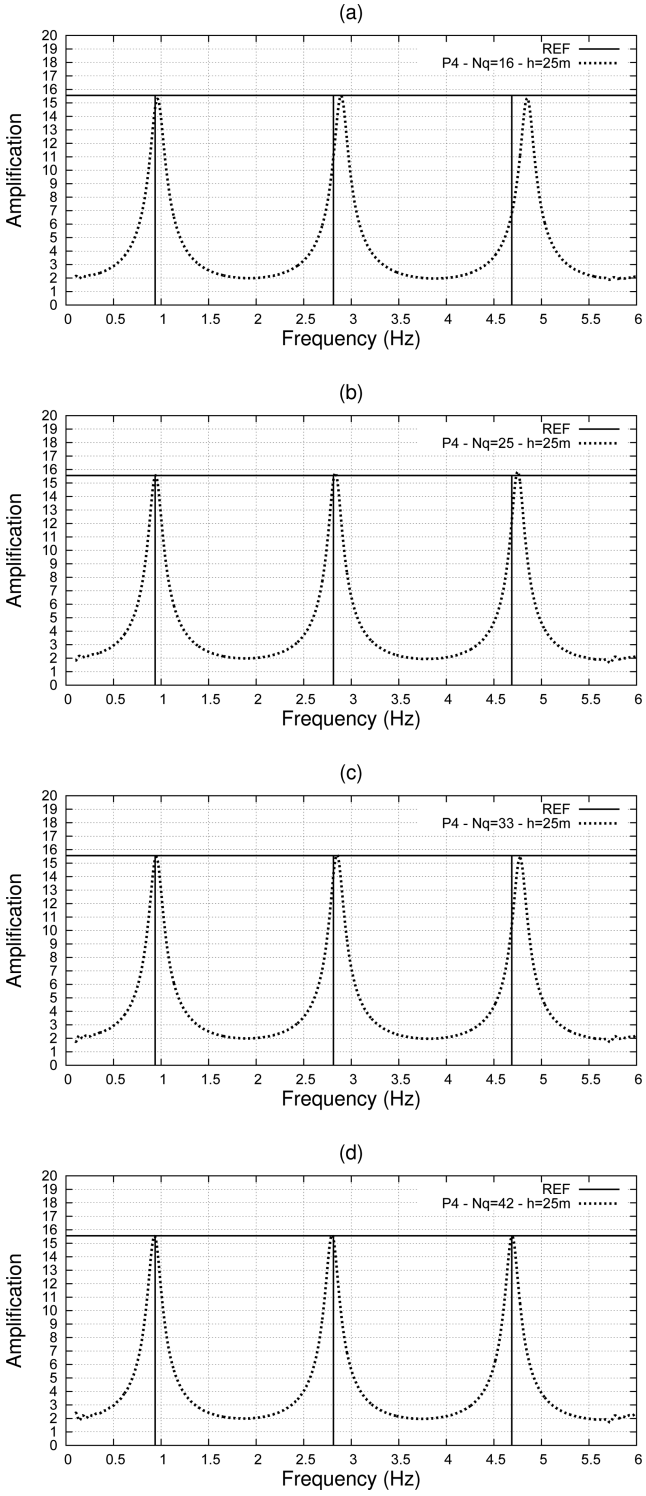

Figure 6. Transfer functions of the horizontal velocity v_x at the surface. Results for the $\mathcal{P}_4$ DG method for $h = 25$ m using (a) $N_q = 16$, (b) $N_q = 25$, (c) $N_q = 33$ and (d) $N_q = 42$ quadrature points for the calculation of the modified mass matrix.

In a first step, we concentrate in the approximation of a smoothly varying velocity model within the basin. Secondly, we test the capability of the presented methodology to deal with strong jumps in material properties within the elements of the mesh, as it has been presented in Section 4.2 for the 1-D-amplification.

The physical domain has a width of 10 km and a depth of 5 km. The basin bottom is represented by a trapezoidal shape of 4000 m at the surface, 2800 m at the bottom base located at 300 m depth (see Fig. 8). The velocity model within the basin consists of a linear gradient with increasing velocities from $v_S = 500$ m s^{-1} at the surface down to $v_S = 900$ m s^{-1} at the basin bottom (we assume a constant Poisson ratio $\nu = 0.25$) and a constant density of $\rho = 2000$ kg m^{-3}. The rock substratum properties are set to $v_P = 4000$ m s^{-1}, $v_S = 2600$ m s^{-1} and $\rho = 2500$ kg m^{-3}. The discretization is composed of 6835 straight-sided triangles, ranging from 40 m on top and 80 m at the bottom of the basin, and a polynomial degree of order 4 is used for the interpolation within each triangle. This assures accurate simulations up to around 10 Hz (i.e. minimum wavelength of 50 m at the top of the model). We use a quadrature rule of order 10 ($N_q = 25$ quadrature points per element) accurate enough for the interpolation degree used. The numerical mesh shown in Fig. 8 has a free surface condition on the top edge and absorbing boundaries at the left, right and bottom edges. In order to excitate different waves in the basin, we perturb the medium with a point (explosive) source located at $X = 5027$ m, and $Z = 3061$ m, modulated in time by a Gaussian wavelet with central frequency $f_0 = 4$ Hz. Receivers are placed at the top edge of the model from $X = 2500$ m to $X = 7500$ m.

First of all, we compare the DG solution with a reference solution calculated by the open-source SPECFEM2D package (available from http://www.geodynamics.org) based on the spectral element method (SEM) and widely used by the seismological community (Komatitsch & Vilotte 1998; Tromp *et al.* 2008, and references therein). The spectral element mesh is composed of 6797 quadrilaterals and respects the boundary of the basin. A multidimensional lagrangian interpolation of degree 4 is used. This mesh deliberately oversamples the wavefield for the current velocity model and a simulation up to 10 Hz maximum frequency. We run exactly the same simulation and the results can be seen in the trace panels of Fig. 10. We can hardly see any difference between the seismograms of the horizontal components calculated by both methodologies (similar results for the vertical component not shown here). Therefore we verify that the proposed DG methodology generates reliable results for a complex wavefield in a smoothly varying medium.

In a second stage, we evaluate the improvement brought by the new DG methodology by comparing with the results obtained using a classical piecewise constant approximation for the velocity gradient inside the sedimentary basin. In Fig. 9, we can see the approximation of the velocity gradient in the basin by a piecewise constant approximation inside each element (a) and by the *true* velocity model evaluated at the quadrature points (b). We now compare the DG solution against the reference solution calculated by

Table 7. Accuracy of the $\mathcal{P}_4$ DG method for transfer functions when the mesh does not honour the discontinuity between the media ($h = 25$ m, mesh contains 480 triangles). Values of amplification $a(i)$, corresponding frequency $f(i)$ (in Hz) for $i = 1, \ldots, 3$ and relative errors (in per cent) with respect to the theoretical values for $N_q = 16, 25, 33$ and 42.

N_q	CPU (s)	$a(1)$	$err_a(1)$ (per cent)	$f(1)$ (Hz)	$err_f(1)$ (per cent)	$a(2)$	$err_a(2)$ (per cent)	$f(2)$ (Hz)	$err_f(2)$ (per cent)	$a(3)$	$err_a(3)$ (per cent)	$f(3)$ (Hz)	$err_f(3)$ (per cent)
16	236	15.2929	1.7	0.9625	2.7	15.5315	0.1	2.8925	2.8	15.3408	1.4	4.8500	3.5
25	231	15.5522	0.02	0.9425	0.5	15.7530	1.3	2.8325	0.7	15.8394	1.8	4.7500	1.3
33	230	15.4594	0.6	0.9475	1.1	15.6042	0.3	2.8500	1.3	15.3933	1.0	4.6650	1.9
42	230	15.5258	0.2	0.9325	0.5	15.6119	0.4	2.7974	0.5	15.5174	0.2	4.6925	0.1

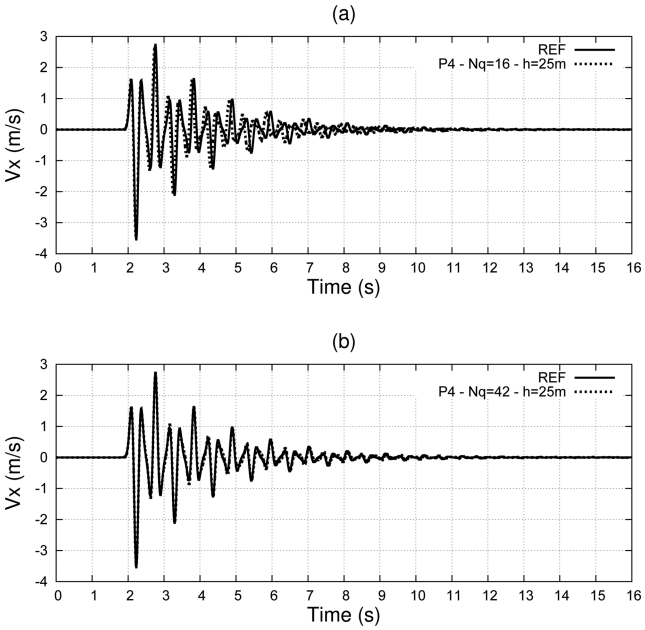

Figure 7. Time evolution of the horizontal velocity v_x at the surface. Results for the $\mathcal{P}_4$ DG method for $h = 25$ m using (a) $N_q = 16$ and (b) $N_q = 42$ quadrature points for the calculation of the modified mass matrix.

the SEM in Fig. 11(a) where we can clearly see the differences, specially in the surface waves trapped inside the basin. This highlights the difficulty for the previous constant-by-element DG approach to accurately reproduce the surface wave dispersion due to the sedimentary basin, unless an extreme refinement of the mesh near the free-surface of the model and inside the basin is used.

In order to emphasize the previous effect, we run the same example but coarsening the mesh as much as possible. We create a mesh of 5562 straight-sided triangles with an edge size of 50 m on the top and 100 m at the bottom of the basin for the same gradient velocity model, and we use interpolation polynomials of degree 5. We then obtain an accurate simulation for wavelengths down to 50 m. We now consider a quadrature formula of order 12 ($N_q = 33$) to take into account the interpolation degree of 5 and also the velocity variations inside the elements. Again we run two simulations: one with the current methodology and an other one with the previous constant-by-element discretization of the velocity model. The differences shown in Fig. 11(b) are larger than in the previous case, as expected because of the coarsening of the mesh. Note however that this is not caused by an insufficient sampling of the wavefield (i.e. classical numerical dispersion), but merely due to the limited representation of the velocity gradient inside the basin. To better quantify the differences, we show in Fig. 12 the traces from the surface receiver at $X = 3200$ m (marked by an arrow in the panels of Fig. 10). The comparisons are quantified with the time frequency misfit criteria of Kristeková *et al.* (2009). First, we confirm that using the new DG method both meshes accurately reproduce the reference seismograms calculated by SEM. Moreover, the results corresponding to the higher degree polynomial interpolation (degree 5) are even better, which proves the interest for high order interpolations even when associated to the standard leap-frog time scheme. Secondly, we clearly see that the errors are quite large when using the constant-by-element velocity discretization, reaching almost 50 per cent for the later surface wave arrivals, and becoming worse with the mesh coarsening.

Lastly and following a reviewer's suggestion, we decide to test the capability of the method to reproduce the 2-D complex wavefield without honouring the geological interface between the basin bottom and the bedrock. At a first glance, this is not an easy task as the ratio in material impedance is of the order of 3.6. We create a mesh which satisfies the sampling criteria of the wavefield with interpolation polynomials of degree 5 and we run two cases: one with the quadrature formula of order 12 ($N_q = 33$) and the other with the quadrature formula of order 14 ($N_q = 42$). We do not apply any interface constraint in the mesh generation process, and therefore it does not match the interface between the basin and the bedrock, as we can see in Fig. 13. From the trace panels shown in Fig. 14, we can conclude that even without honouring the bottom of the basin, the method recovers the material variability with a high enough number of quadrature points in the elements sharing the sedimentary layer and the bedrock. We stress however, that a limit will be encountered when the jump in material properties increases, as the quadrature formulas are thought to integer smooth (i.e. polynomial) functions. In Fig. 15, we show the differences of the receiver at $X = 3200$ m for just the horizontal component, similar results are found for the vertical one (not shown here). We clearly appreciate the better accuracy while increasing the number of quadrature points. The envelope and phase misfits are lower than 5 per cent. They are relatively higher than those of Fig. 10(b) (lower than 2 per cent) when the mesh exactly follows the interface between basin and bedrock, as expected. But they are much lower than those shown in Fig. 11(b) (higher than 10 per cent) when the gradient velocity model within the basin was badly represented by the constant-by-element approach.

5 CONCLUSIONS

We present an extension of the high-order nodal DG method based on centred fluxes and a second-order time scheme to elastic media with arbitrary heterogeneities. The objective of this extension is to relax the assumption of constant material properties within the elements of the mesh without loosing the high-order accuracy of the method, and with only minor modifications to the actual DG scheme. This is possible by the introduction of a change of variable for the stress components which allows writing the elastodynamic system in pseudo-conservative form where the material parameters appear only as coefficients of the time derivatives. As a consequence, the

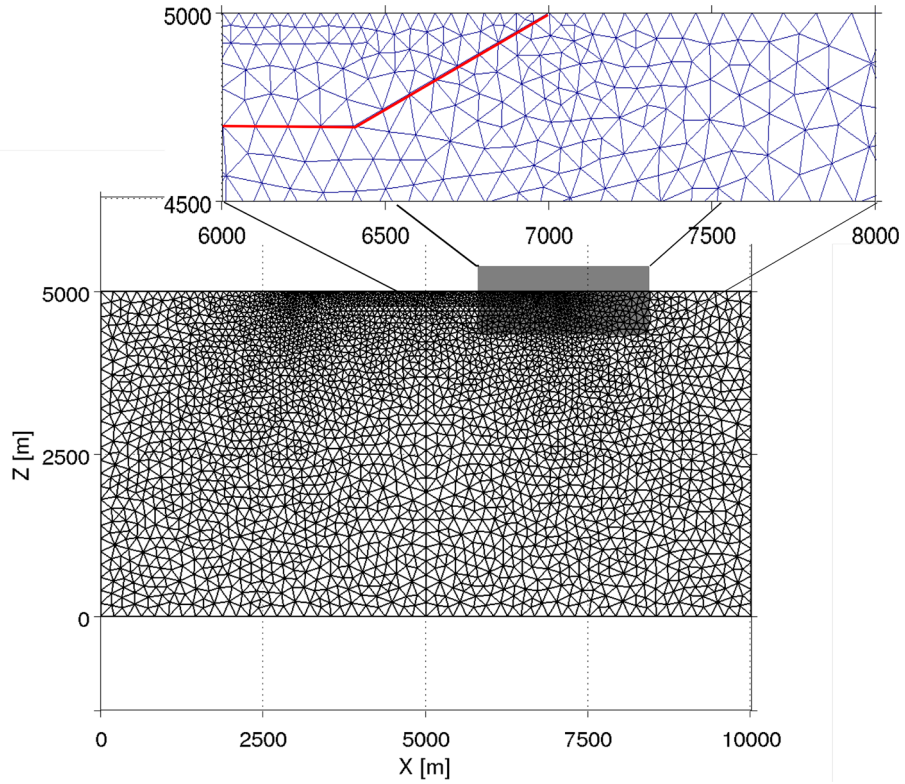

Figure 8. Triangular mesh of the sedimentary basin model of 5562 elements, 50 m minimum edge at the top edge of the model.

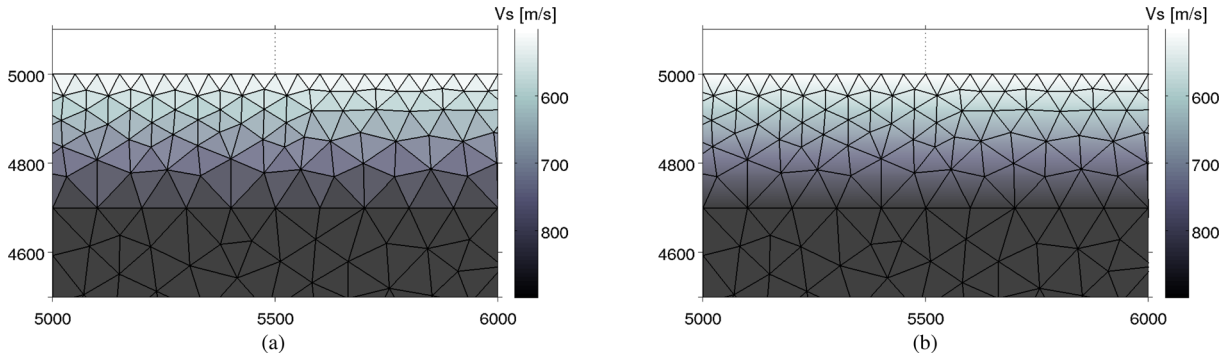

Figure 9. Detail of the velocity gradient discretization of the sedimentary basin: (a) classical piecewise constant velocities per triangle and (b) *true* gradient velocity model that is evaluated at each quadrature point.

introduction of variable properties inside elements reduces to the calculation of modified mass matrices. This is done by resorting to another set of quadrature points, where the material properties need to be assigned, that is different from the nodal set of interpolation points. The interconnection between both set of points is established by generalized Vandermonde matrices evaluated at each nodal set. We verified first the *hp*-convergence of the presented methodology for a smoothly varying media. As the interpolation order increases, the error decreases with the order of the time scheme, as expected. Moreover, except for very coarse meshes, the convergence and the error levels are comparable to the results obtained for a homogeneous medium. To obtain satisfactory results for a simulation with interpolation order p, the order of the quadrature formula needs to be at least $2p$ for smoothly varying material properties within the elements.

In the case of strong impedance contrasts, we show the advantages of the new DG methodology to calculate the surface amplification due to a soft layer near the free surface, in terms of reduced complexity in mesh generation and computational efficiency provided by the high-order interpolation. Very accurate results are obtained using meshes that do not follow the strong jump between material properties. In this case, it is essential to increase the number of quadrature points (using quadrature formulas of order greater than $2p$) in order to better sample the discontinuity in material properties within the elements. Moreover, the method appears to be very flexible since the number of quadrature points can be increased if necessary, independently of the set of interpolation nodes. Nevertheless, a limit is readily reached in the integral approximation as the quadrature formulae used are meant to accurately integrate smooth functions.

We compare the simulation results against solutions calculated by the SEM for a more realistic 2-D basin example and prove the applicability of the DG extension to more complex heterogeneous configurations. The results confirm the difficulty for the

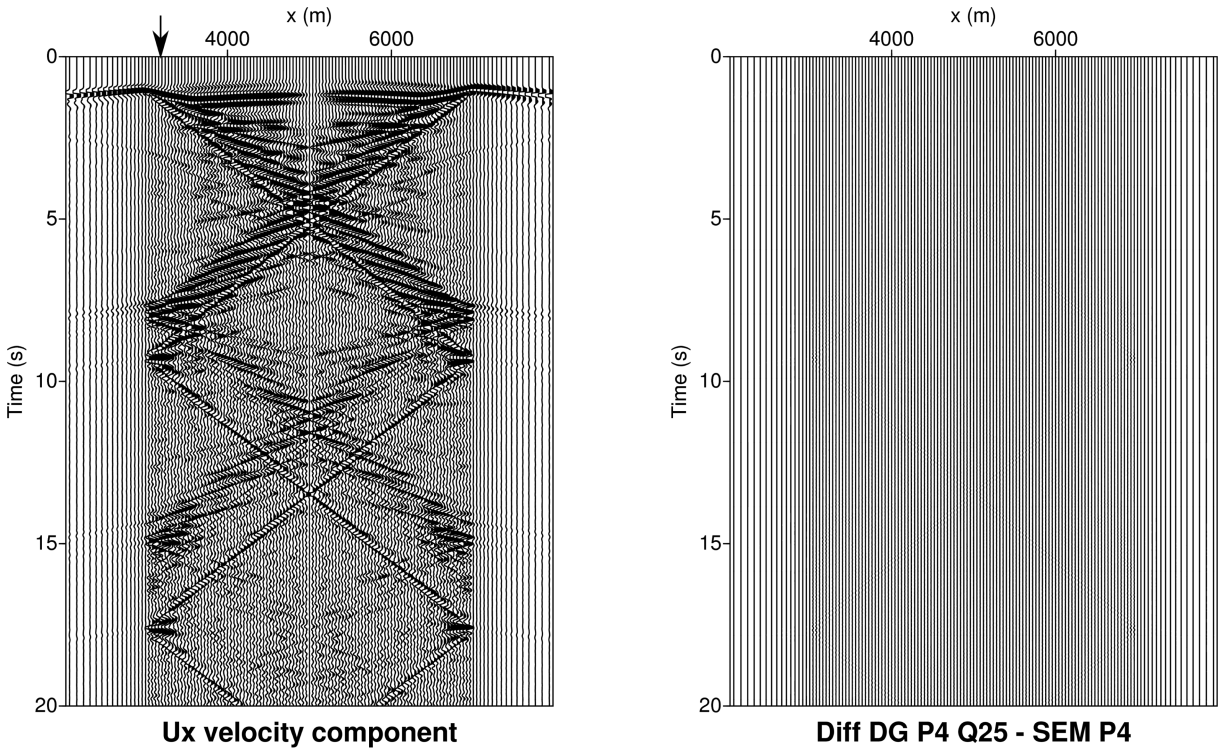

(a) (b)

Figure 10. Seismograms of horizontal velocity components. (a) calculated by the new DG method and (b) differences with respect to the SPECFEM2D calculation (same amplitude scale). Vertical arrow at $X = 3200$ m indicating the receiver analysed later.

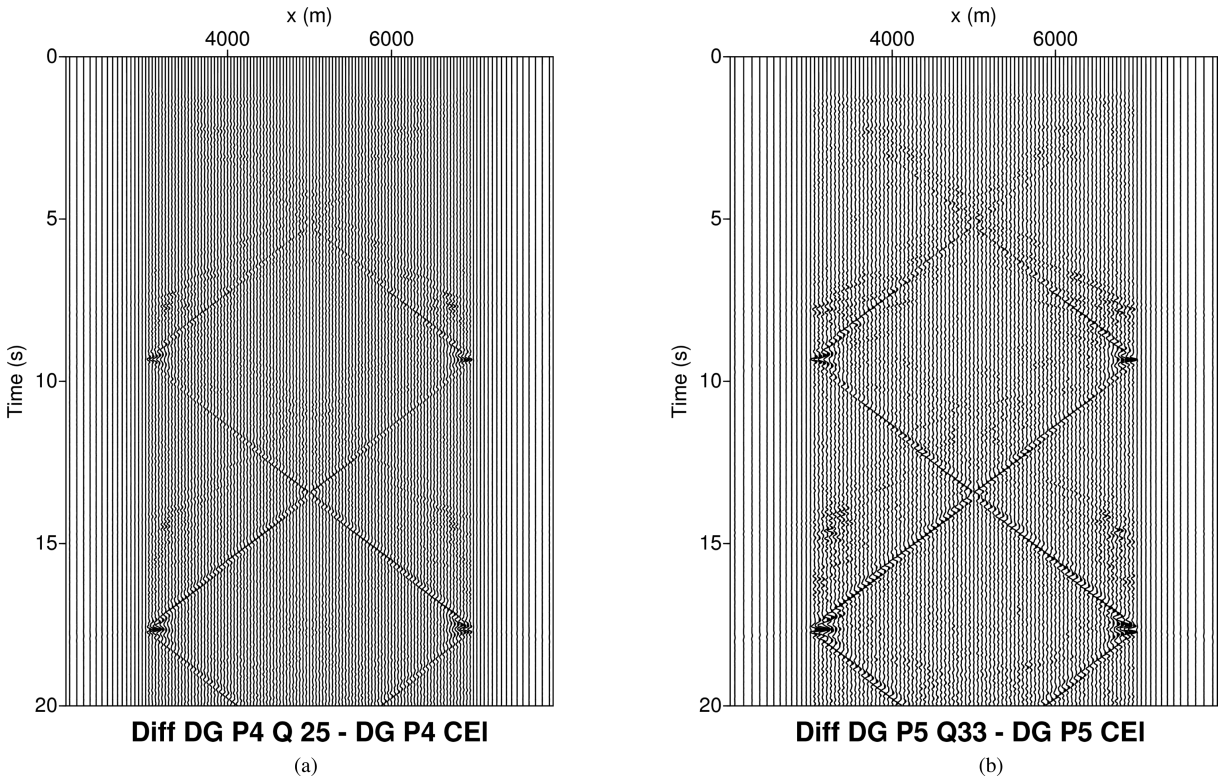

(a) (b)

Figure 11. Differences between classical CEl (constant-by-element) DG method and the new methodology (based on modified mass matrices) of horizontal velocity seismograms for: (a) a mesh of 40 m at the surface, polynomial degree $\mathcal{P}_4$, and 25 quadrature points, and (b) a mesh of 50 m at the surface, polynomial degree $\mathcal{P}_5$, and 33 quadrature points.

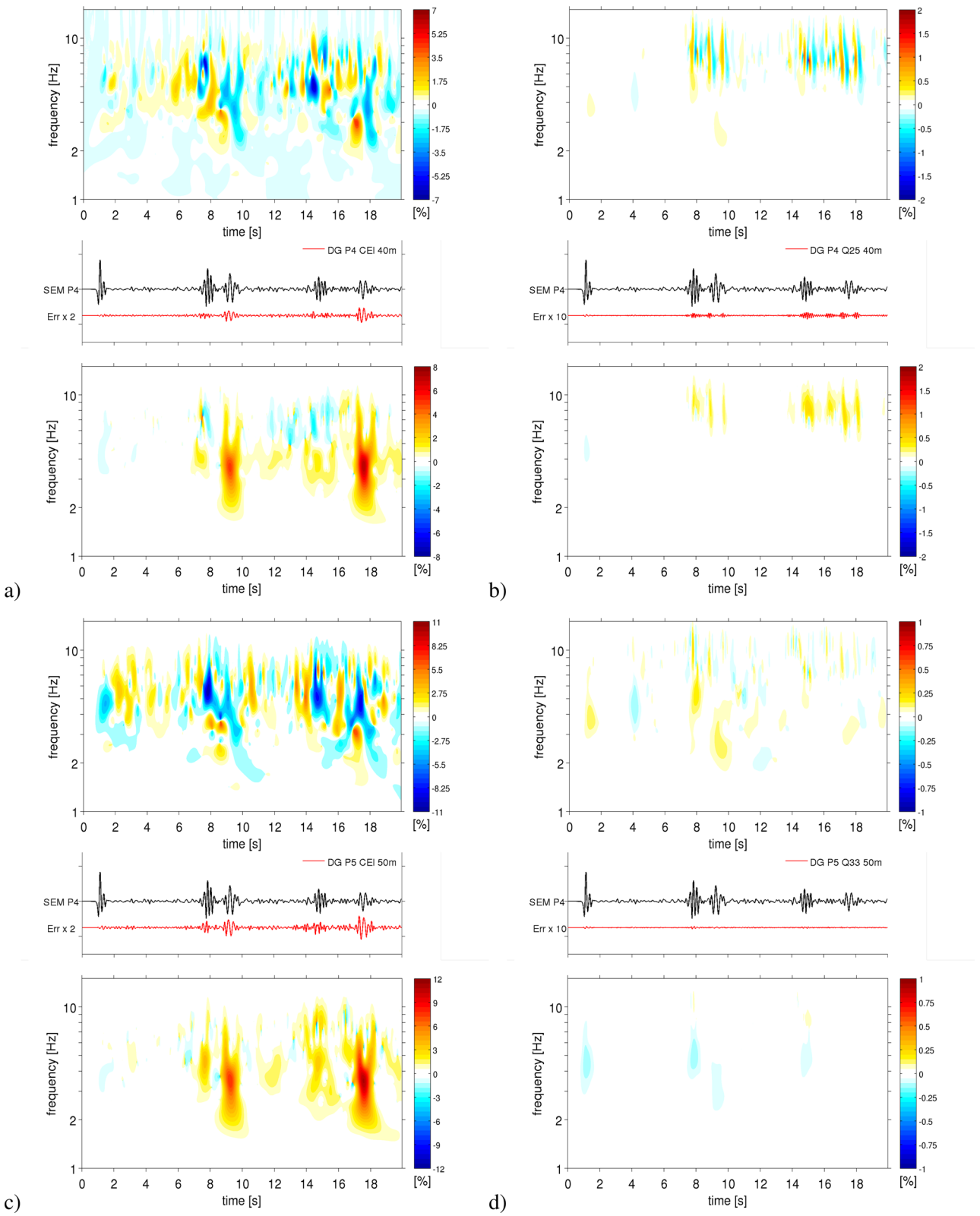

Figure 12. Seismograms (horizontal component) of receiver at $X = 3200$ m comparing differences to the reference SPECFEM2D solution for the classical CEI (constant-by-element) DG method and the new methodology for: (a) the mesh of 40 m, polynomial degree $\mathcal{P}_4$ with constant by element discretization, (b) the mesh of 40 m, polynomial degree $\mathcal{P}_4$ with 25 quadrature points, (c) the mesh of 50 m, polynomial degree $\mathcal{P}_5$ with constant by element discretization, and (d) the mesh of 50 m, polynomial degree $\mathcal{P}_5$ with 33 quadrature points. The differences are multiplied by a factor of 2 for the constant-by-element cases and by a factor of 10 for the new methodology. Time-Frequency misfit criteria shown on top (envelope misfit) and bottom (phase misfit) of each seismogram (different colourscales for each case).

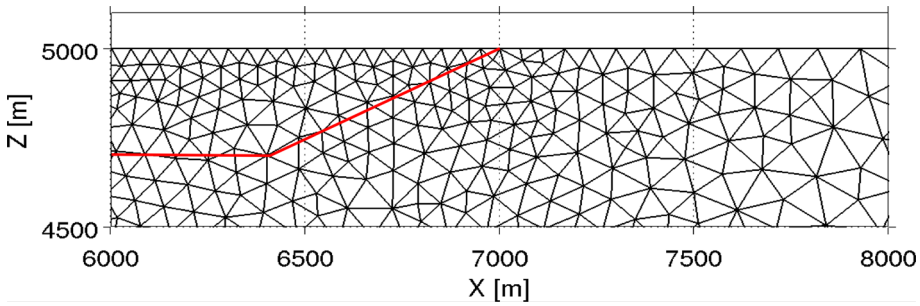

Figure 13. Detail of the triangular mesh at the edge of the sedimentary basin (same inset of Fig. 8). Note that the unstructured mesh does not honour the bottom of the basin (red line).

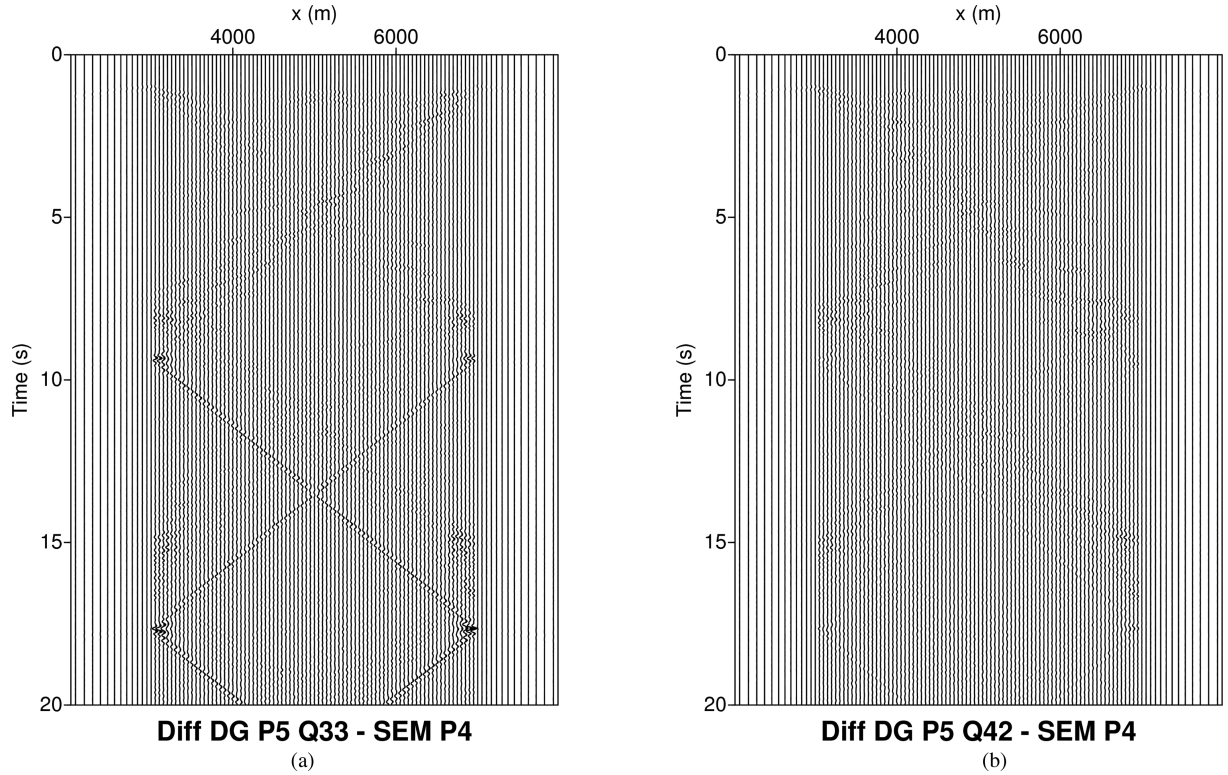

Figure 14. Differences between two runs of the new methodology (based on modified mass matrices) of horizontal velocity seismograms with respect to the reference solution of SPECFEM2D for an arbitrary mesh *not honouring* the basin-bedrock interface with: (a) a polynomial degree $\mathcal{P}_5$ and 33 quadrature points, and (b) the same mesh with a polynomial degree $\mathcal{P}_5$ and 42 quadrature points.

initial method, based on constant material properties per element, to produce accurate solutions for smoothly varying media (such as gradients) unless using extremely refined meshes. Then, we propose the following strategy for any ground motion simulation at the local or regional scales: when the impedance contrasts in the subsurface are highly pronounced (e.g. at the contact between the bottom of the basin and the substratum), the computational mesh should honour the interface as much as possible; on the other hand, when the impedance contrast are not so pronounced or in the case of smooth variations, the proposed DG method can be highly beneficial. It considerably simplifies the mesh generation and allows avoiding small elements that reduce the global time step of simulations.

In addition to the accuracy and the flexibility of the proposed extension, a remarkable property is that it does not increase the computational cost of classical DG schemes with constant material properties per element. The heterogeneity of the medium is only taken into account for the calculation of the modified mass matrices (with arbitrary levels of detail and integration orders) once in a pre-processing stage of the simulation. There is however an increase in storage capacity (i.e. the inverse of the modified mass matrices need to be stored for each element), and the need to access these matrices at each time step during the simulation.

Finally, the choice adopted in this work to solving the elastodynamics system (4) in the pseudo-conservative form is not mandatory, and the proposed methodology can be applied to the original formulation expressed in eq. (2) to account for anelastic and/or anisotropic media. In such cases the rigidity matrices and the numerical fluxes will depend on the variable material properties. Therefore they should also be calculated and stored for each element of the mesh. The computational costs of such approach must be evaluated, specially in the 3-D case. These different topics will be the subject of future research.

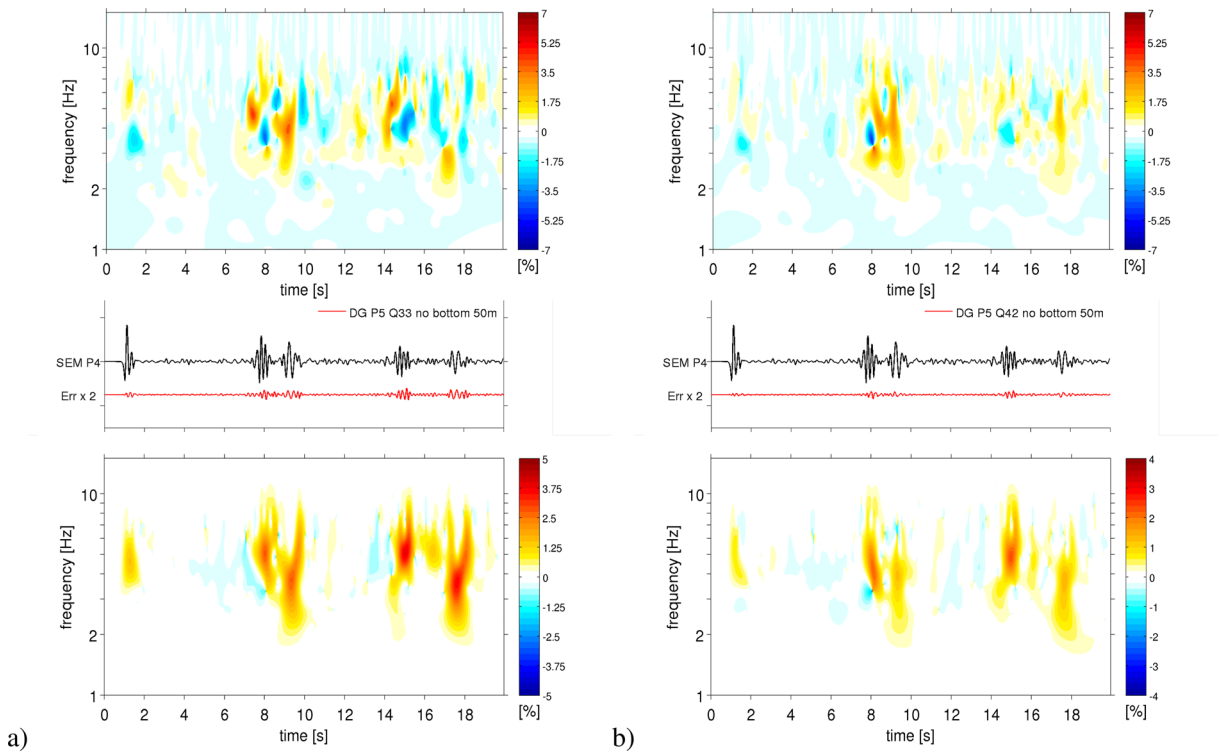

Figure 15. Seismograms (horizontal component) of receiver at $X = 3200$ m comparing differences to the reference SPECFEM2D solution for an arbitrary mesh *not honouring* the basin-bedrock interface with: (a) a polynomial degree $\mathcal{P}_5$ and 33 quadrature points, and (b) the same mesh with a polynomial degree $\mathcal{P}_5$ and 42 quadrature points. Time–frequency misfit criteria shown on top (envelope misfit) and bottom (phase misfit) of each seismogram.

ACKNOWLEDGEMENTS

The authors are very grateful to J. Tago Pacheco and an anonymous reviewer for their constructive remarks that have contributed to improve the quality of the paper.

REFERENCES

Bao, H., Bielak, J., Ghattas, O., Kallivokas, L.F., O'Hallaron, D.R., Shewchuk, J.R. & Xu, J., 1998. Large-scale simulation of elastic wave propagation in heterogeneous media on parallel computers, *Comput. Methods Appl. Mech. Eng.,* **152,** 85–102.

Bard, P.-Y. & Bouchon, M., 1980a. The seismic response of sediment-filled valleys. Part 1: the case of incident SH waves, *Bull. seism. Soc. Am.,* **70,** 1263–1286.

Bard, P.-Y. & Bouchon, M., 1980b. The seismic response of sediment-filled valleys. Part 2: the case of incident P and SV waves, *Bull. seism. Soc. Am.,* **70,** 1921–1941.

Bard, P.-Y. & Bouchon, M., 1985. The two-dimensional resonance of sediment-filled valleys, *Bull. seism. Soc. Am.,* **75,** 519–541.

Benjemaa, M., Glinsky-Olivier, N., Cruz-Atienza, V.M., Virieux, J. & Piperno, S., 2007. Dynamic non-planar crack rupture by a finite volume method, *Geophys. J. Int.,* **171**(1), 271–285.

Benjemaa, M., Glinsky-Olivier, N., Cruz-Atienza, V.M. & Virieux, J., 2009. 3D dynamic rupture simulation by a finite volume method, *Geophys. J. Int.,* **178**(1), 541–560.

Bielak, J., Loukakis, K., Hisada, Y. & Yoshimura, C. 2003. Domain reduction method for three-dimensional earthquake modeling in localized regions. Part I: theory, *Bull. seism. Soc. Am.,* **93,** 817–824.

Canuto, C., Hussaini, M.Y., Quarteroni, A. & Zang, T.A., 1988. *Spectral Methods in Fluid Dynamics,* Springer-Verlag.

Castro, C.E., Käser, M. & Brietzke, G.B., 2010. Seismic waves in heterogeneous material: subcell resolution of the discontinuous Galerkin method, *Geophys. J. Int.,* **182**(1), 250–264.

Cockburn, B., Karniadakis, G.E. & Shu, C.-W., 2000. Discontinuous Galerkin Methods: Theory, Compuration and Applications, Lecture Notes in Computational Sciences and Engineering, Springer.

Cohen, G., Joly, P., Roberts, J. & Tordjman, N., 2001. Higher order triangular finite elements with mass lumping for the wave equation, *SIAM J. Numer. Anal.,* **38**(6), 2047–2078.

Cupillard, P., Delavaud, E., Burgos, G., Festa, G., Vilotte, J.-P., Capdeville, Y. & Montagner, J.-P., 2012. RegSEM: a versatile code based on the spectral element method to compute seismic wave propagation at the regional scale, *Geophys. J. Int.,* **188**(3), 1203–1220.

De Basabe, J.D. & Sen, M.K., 2007. Grid dispersion and stability criteria of some common finite-element methods for acoustic and elastic wave equations, *Geophysics,* **72**(6), T81–T95.

De Basabe, J.D., Sen, M.K. & Wheeler, M.F., 2008. The interior penalty discontinuous Galerkin method for elastic wave propagation: grid dispersion, *Geophys. J. Int.,* **175**(1), 83–93.

de la Puente, J., Käser, M., Dumbser, M. & Igel, H., 2007. An arbitrary high-order discontinuous Galerkin method for elastic waves on unstructured meshes – IV. Anisotropy, *Geophys. J. Int.,* **169**(3), 1210–1228.

De Martin, F., 2011. Verification of a spectral-element method code for the Southern California Earthquake Center LOH.3 viscoelastic case, *Bull. seism. Soc. Am.,* **101**(6), 2855–2865.

Delcourte, S. & Glinsky, N., 2015. Analysis of a high-order space and time discontinuous Galerkin method for elastodynamic equations. application to 3D wave propagation, *ESAIM Math. Mod. Numer. Anal.,* in press.

Delcourte, S., Fezoui, L. & Glinsky, N., 2009. A high-order discontinuous Galerkin method for the seismic wave propagation, in *ESAIM Proceedings,* Vol. 27, pp. 70–89.

Dubiner, M., 1991. Spectral methods on triangles and other domains, *J. Sci. Comput.,* **6,** 345–390.

Dumbser, M. & Käser, M., 2006. An arbitrary high-order discontinuous Galerkin method for elastic waves on unstructured meshes – II: the three-dimensional isotropic case, *Geophys. J. Int.,* **167**(1), 319–336.

Dumbser, M., Käser, M. & Toro, E., 2007. An arbitrary high order Discontinuous Galerkin method for elastic waves on unstructured

meshes – V. Local time stepping and p-adaptivity, *Geophys. J. Int.,* **171**(2), 695–717.

Dunavant, D.A., 1985. High degree efficient symmetrical Gaussian quadrature rules for the triangle, *Int. J. Numer. Methods Eng.,* **21,** 1129–1148.

Etienne, V., Chaljub, E., Virieux, J. & Glinsky, N., 2010. An hp-adaptive discontinuous Galerkin finite-element method for 3D elastic wave modelling, *Geophys. J. Int.,* **183**(2), 941–962.

Faccioli, E., Maggio, F., Paolucci, R. & Quarteroni, A., 1997. 2D and 3D elastic wave propagation by a pseudo-spectral domain decomposition method, *J. Seismol.,* **1,** 237–251.

Hermann, V., Käser, M. & Castro, C.E., 2011. Non-conforming hybrid meshes for efficient 2-D wave propagation using the discontinuous Galerkin method, *Geophys. J. Int.,* **184**(2), 746–758.

Hesthaven, J.S. & Teng, C.H., 2000. Stable spectral methods on tetrahedral elements, *SIAM J. Sci. Comput.,* **21**(6), 2352–2380.

Hesthaven, J.S. & Warburton, T., 2008. *Nodal Discontinuous Galerkin Methods: Algorithms, Analysis, and Applications,* Vol. 54 of Texts in Applied Mathematics, Springer.

Karniadakis, G. & Sherwin, S., 1999. *Spectral/hp Element Methods for Continuum Fluid Dynamics,* Cambridge Univ. Press.

Käser, M. & Dumbser, M., 2006. An arbitrary high order discontinuous Galerkin method for elastic waves on unstructured meshes – I: the two-dimensional isotropic case with external source terms, *Geophys. J. Int.,* **166**(2), 855–877.

Käser, M., Dumbser, M., De La Puente, J. & Igel, H., 2007a. An arbitrary high-order discontinuous Galerkin method for elastic waves on unstructured meshes – III. Viscoelastic attenuation, *Geophys. J. Int.,* **168**(1), 224–242.

Käser, M., Mai, P.M. & Dumbser, M., 2007b. Accurate calculation of fault-rupture models using the high-order discontinuous galerkin method on tetrahedral meshes, *Bull. seism. Soc. Am.,* **97**(5), 1570–1586.

Komatitsch, D. & Vilotte, J.P., 1998. The spectral-element method: an efficient tool to simulate the seismic response of 2D and 3D geological structures, *Bull. seism. Soc. Am.,* **88**(2), 368–392.

Komatitsch, D., Martin, R., Tromp, J., Taylor, M.A. & Wingate, B.A., 2001. Wave propagation in 2-D elastic media using a spectral element method with triangles and quadrangles, *J. Comput. Acoust.,* **9**(2), 703–718.

Koorwinder, T., 1975. Two-variable analogues of the classical orthogonal polynomials, in *Theory and Applications of Special Functions,* pp. 435–495, ed. Askey, R.A., Academic Press.

Kramer, S., 1996. *Geothecnical Earthquake Engineering,* Prentice Hall International.

Kristeková, M., Kristek, J. & Moczo, P., 2009. Time-frequency misfit and goodness-of-fit criteria for quantitative comparison of time signals, *Geophys. J. Int.,* **178,** 813–825.

Lazar, L., Pasquetti, R. & Rapetti, F., 2013. Fekete-Gauss finite elements for incompressible Navier-Stokes flows, *Commun. Comput. Phys.,* **13**(5), 1309–1329.

Liu, T., Sen, M.K., Hu, T., De Basabe, J.D. & Li, L., 2012. Dispersion analysis of the spectral element method using a triangular mesh, *Wave Motion,* **49**(4), 474–483.

Mazzieri, I. & Rapetti, F., 2012. Dispersion analysis of triangle-based spectral element methods for elastic wave propagation, *Numer. Algorith.,* **60,** 631–650.

Mazzieri, I., Stupazzini, M., Guidotti, R. & Smerzini, C., 2013. SPEED: SPectral Elements in Elastodynamics with Discontinuous Galerkin: a non-conforming approach for 3D multi-scale problems, *Int. J. Numer. Methods Eng.,* **95**(12), 991–1010.

Mercerat, E.D., Vilotte, J.P. & Sánchez-Sesma, F., 2006. Triangular spectral element simulation of 2D elastic wave propagation using unstructured triangular grids., *Geophys. J. Int.,* **166,** 679–698.

Moczo, P., Kristek, J. & Gális, M., 2014. *The Finite-Difference Modelling of Earthquake Motions: Waves and Ruptures,* Cambridge Univ. Press.

Olsen, K.B., Day, S.M., Minster, J.B., Cui, Y., Chourasia, A., Okaya, D., Maechling, P. & Jordan, T., 2008. Terashake2: spontaneous rupture simulations of Mw 7.7 earthquakes on the Southern San Andreas Fault, *Bull. seism. Soc. Am.,* **98**(3), 1162–1185.

Owens, R.G., 1998. Spectral approximation on the triangle, *Proc. R. Soc. Lond., A,* **454,** 857–872.

Pasquetti, R. & Rapetti, F., 2006. Spectral element methods on unstructured meshes: comparisons and recent advances, *J. Sci. Comput.,* **27**(1–3), 377–387.

Pasquetti, R. & Rapetti, F., 2010. Spectral element methods on unstructured meshes: which interpolation points?, *Numer. Algorith.,* **55**(2), 349–366.

Peter, D. *et al.*, 2011. Forward and adjoint simulations of seismic wave propagation on fully unstructured hexahedral meshes, *Geophys. J. Int.,* **186**(2), 721–739.

Peyrusse, F., Glinsky, N., Gélis, C. & Lanteri, S., 2014. A nodal discontinuous Galerkin method for site effects assessment in viscoelastic mediaverification and validation in the Nice basin, *Geophys. J. Int.,* **199**(1), 315–334.

Proriol, J., 1957. Sur une famille de polynomes à deux variables orthogonaux dans un triangle, *C. R. Acad. Sci. Paris,* **245,** 2459–2461.

Robertsson, J.O.A., Bednar, B., Blanch, J., Kostov, C. & van Manen, D.-J., 2007. Introduction to the supplement on seismic modeling with applications to acquisition, processing, and interpretation, *Geophysics,* **72**(5), SM1–SM4.

Sánchez-Sesma, F.J. & Luzón, F., 1995. Seismic response of three-dimensional alluvial valleys for incident P, S, and Rayleigh waves, *Bull. seism. Soc. Am.,* **85**(1), 269–284.

Seriani, G. & Oliveira, S.P., 2008. Dispersion analysis of spectral elements methods for elastic wave propagation, *Wave Motion,* **45,** 729–744.

Seriani, G. & Priolo, E., 1994. Spectral element method for acoustic wave simulation in heterogeneous media, *Finite Elements Anal. Des.,* **16**(34), 337–348.

Seriani, G. & Su, C., 2012. Wave propagation modeling in highly heterogeneous media by a poly-grid Chebyshev spectral element method, *J. Comp. Acous.,* **20**(02), 1240004, doi:10.1142/S0218396X12400048.

Sherwin, S. & Karniadakis, G., 1995. A new triangular and tetrahedral basis for high-order finite element methods, *Int. J. Numer. Meth. Eng.,* **38**(2), 3775–3802.

Stupazzini, M., Paolucci, R. & Igel, H., 2009. Near-fault earthquake ground-motion simulation in the Grenoble Valley by a high-performance spectral element code, *Bull. seism. Soc. Am.,* **99**(1), 286–301.

Taborda, R., Bielak, J. & Restrepo, D., 2012. Earthquake groundmotion simulation including nonlinear soil effects under idealized conditions with application to two case studies, *Seism. Res. Lett.,* **83**(6), 1047–1060.

Tago, J., Cruz-Atienza, V.M., Virieux, J., Etienne, V. & Sánchez-Sesma, F.J., 2012. A 3D hp-adaptive discontinuous Galerkin method for modeling earthquake dynamics, *J. geophys. Res.: Solid Earth,* **117**(B9), doi:10.1029/2012JB009313.

Taylor, M.A., Wingate, B.A. & Vincent, R.E., 2000. An algorithm for computing Fekete points in a triangle, *SIAM J. Numer. Anal.,* **38**(5), 1707–1720.

Tromp, J., Komatitsch, D. & Liu, Q., 2008. Spectral-element and adjoint methods in seismology, *Commun. Comput. Phys.,* **3,** 1–32.

Virieux, J., 1986. P-SV wave propagation in heterogeneous media, velocity-stress finite difference method, *Geophysics,* **51,** 889–901.

Virieux, J. *et al.*, 2012. Modelling Seismic Wave Propagation for Geophysical Imaging, *Seismic Waves – Research and Analysis,* Chapter 13, pp. 253–304, ed. Kanao, M., InTech.

Warburton, T., 2006. An explicit construction of interpolation nodes on the simplex, *J. Eng. Math.,* **56,** 247–262.

Warburton, T., Pavarino, L. & Hesthaven, J.S., 2000. A pseudo-spectral scheme for the incompressible Navier-Stokes equations using unstructured nodal elements, *J. Comput. Phys.,* **164,** 1–21.

Wenk, S., Pelties, C., Igel, H. & Käser, M., 2013. Regional wave propagation using the discontinuous Galerkin method, *Solid Earth,* **4**(1), 43–57.

Wu, R.-S., Maupin, V. & Dmowska, R., 2007. *Advances in Wave Propagation in Heterogenous Earth,* Elsevier.

Xu, J., Bielak, J., Ghattas, O. & Wang, J., 2003. Three-dimensional nonlinear seismic ground motion modeling in inelastic basins, *Phys. Earth planet. Inter.,* **137**(1–4), 81–95.

Young, J.L., 2001. High-order leap-frog methodology for the temporally dependent Maxwell's equations, *Radio Sci.,* **36,** 9–17.

APPENDIX A: SOURCE TERMS FOR THE CONVERGENCE STUDY IN HETEROGENEOUS MEDIA

When we consider a smoothly varying medium given by $\rho = 1$ kg m^{-3}, $\lambda = 2 + 0.5\sin(2\pi x + 2\pi y)$ kg m^{-1} s^2 and $\mu = 2$ kg m^{-1} s^2, the plane wave defined by

$$\vec{W}^{ex}(x, y, t) = \vec{R}_s\, S_s + \vec{R}_p\, S_p \tag{A1}$$

with

$$S_S = \sin(2\pi x + 2\pi y + 2\sqrt{2}\,\pi\, v_S\, t)\,,$$

$$S_P = \sin(2\pi x + 2\pi y - 2\sqrt{2}\,\pi\, v_P\, t)\,,$$

and

$$\vec{R}_S = \left(\frac{\sqrt{2}}{2}\, v_S,\ -\frac{\sqrt{2}}{2}\, v_S,\ 0,\ \mu,\ 0\right)^t \quad \text{and}$$

$$\vec{R}_P = \left[\frac{\sqrt{2}}{2}\, v_P,\ \frac{\sqrt{2}}{2}\, v_P,\ -(\lambda + 2\mu),\ 0,\ -\mu\right]^t,$$

is no more an exact solution of the pseudo-conservative system

$$\Lambda(\rho, \lambda, \mu)\ \partial_t \vec{\tilde{W}} + \tilde{A}_x \partial_x \vec{\tilde{W}} + \tilde{A}_y \partial_y \vec{\tilde{W}} = \vec{0}\,. \tag{A2}$$

As it is not an easy task to establish a solution of the system including the variations of λ, a classical way consists to solve a modified set of equations containing corrective source terms, as done for instance in (Castro *et al.* 2010),

$$\Lambda(\rho, \lambda, \mu)\ \partial_t \vec{\tilde{W}} + \tilde{A}_x \partial_x \vec{\tilde{W}} + \tilde{A}_y \partial_y \vec{\tilde{W}} = \vec{\mathcal{S}}\,,$$

for which $\vec{W}^{ex}$ is still an exact solution. The components of the corrective source term $\vec{\mathcal{S}}$ are obtained by injecting the expression of $\vec{W}^{ex}$ in each line of the system (A2) and collecting the remaining terms. These terms depend on the derivatives of λ and v_P with respect to x and y which can be gathered in two terms,

$$\partial\lambda = \partial_x\lambda = \partial_y\lambda = \pi\, \cos(2\pi x + 2\pi y)\,,$$

$$\partial v_P = \partial_x v_P = \partial_y v_P = \frac{\cos(2\pi x + 2\pi y)}{2\, v_P}\,.$$

Then, each component of $\vec{\mathcal{S}}$ is calculated

$$\begin{aligned}\mathcal{S}_1 &= \rho\, \partial_t v_x - \partial_x(\sigma_1 + \sigma_2) - \partial_y \sigma_{xy} \\ &= \partial\lambda\, S_P - 2\pi\sqrt{2}\,(\lambda + 2\mu)\, \partial v_P\, t\, C_p\,,\end{aligned}$$

where

$$C_P = \cos(2\pi x + 2\pi y - 2\sqrt{2}\, v_P\, t)\,.$$

In the same way,

$$\begin{aligned}\mathcal{S}_2 &= \rho\, \partial_t v_y - \partial_x \sigma_{xy} - \partial_y(\sigma_1 - \sigma_2) \\ &= \partial\lambda\, S_P - 2\pi\sqrt{2}\,(\lambda + 2\mu)\, \partial v_P\, t\, C_P = \mathcal{S}_1\,,\end{aligned}$$

$$\begin{aligned}\mathcal{S}_3 &= \frac{1}{\lambda + \mu}\, \partial_t \sigma_1 - \partial_x v_x - \partial_y v_y \\ &= (-\sqrt{2}\, S_P + 4\,\pi\, v_P\, t\, C_P)\, \partial v_P\,,\end{aligned}$$

$$\mathcal{S}_4 = \frac{1}{\mu}\partial_t \sigma_2 - \partial_x v_x + \partial_y v_y = 0\,,$$

$$\begin{aligned}\mathcal{S}_5 &= \frac{1}{\mu}\, \partial_t \sigma_{xy} - \partial_x v_y - \partial_y v_x \\ &= (-\sqrt{2}\, S_P + 4\,\pi\, v_P\, t\, C_P)\, \partial v_P\ = \mathcal{S}_3\,.\end{aligned}$$